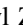



















# Dark Comets? Unexpectedly Large Nongravitational Accelerations on a Sample of Small Asteroids

Darryl Z. Seligman<sup>1</sup> , Davide Farnocchia<sup>2</sup> , Marco Micheli<sup>3</sup> , David Vokrouhlický<sup>4</sup> , Aster G. Taylor<sup>5</sup> , Steven R. Chesley<sup>2</sup> , Jennifer B. Bergner<sup>6</sup> , Peter Veres<sup>7</sup> , Olivier R. Hainaut<sup>8</sup> , Karen J. Meech<sup>9</sup> , Maxime Devogele<sup>10</sup> , Petr Pravec<sup>11</sup> , Rob Matson<sup>12</sup>, Sam Deen<sup>12</sup>, David J. Tholen<sup>9</sup> , Robert Weryk<sup>13</sup> , Edgard G. Rivera-Valentín<sup>14</sup> , and Benjamin N. L. Sharkey<sup>15</sup> 

<sup>1</sup> Department of Astronomy and Carl Sagan Institute, Cornell University, 122 Sciences Drive, Ithaca, NY 14853, USA; [dzs9@cornell.edu](mailto:dzs9@cornell.edu)

<sup>2</sup> Jet Propulsion Laboratory, California Institute of Technology, 4800 Oak Grove Drive, Pasadena, CA 91109, USA

<sup>3</sup> ESA NEO Coordination Centre, Largo Galileo Galilei 1, I-00044 Frascati (RM), Italy

<sup>4</sup> Institute of Astronomy, Charles University, V Holešovičkách 2, CZ-18000 Prague 8, Czech Republic

<sup>5</sup> Department of Astronomy and Astrophysics, University of Chicago, 5640 South Ellis Avenue, Chicago, IL 60637, USA

<sup>6</sup> University of Chicago, Department of the Geophysical Sciences, Chicago, IL 60637, USA

<sup>7</sup> Harvard-Smithsonian Center for Astrophysics, Minor Planet Center, 60 Garden Street, Cambridge, MA 02138, USA

<sup>8</sup> European Southern Observatory, Karl-Schwarzschild-Strasse 2, Garching bei München, D-85748, Germany

<sup>9</sup> Institute for Astronomy, University of Hawaii, 2680 Woodlawn Drive, Honolulu, HI 96822, USA

<sup>10</sup> Arecibo Observatory, University of Central Florida, HC-3 Box 53995, Arecibo, PR 00612, USA

<sup>11</sup> Astronomical Institute, Academy of Sciences of the Czech Republic, Fričova 1, CZ-25165 Ondřejov, Czech Republic

<sup>12</sup> Veneto Observatory, 1 Veneto, Newport Coast, CA 92657, USA

<sup>13</sup> Physics and Astronomy, The University of Western Ontario, 1151 Richmond Street, London, ON N6A 3K7, Canada

<sup>14</sup> Johns Hopkins University Applied Physics Laboratory, 11100 Johns Hopkins Road, Laurel, MD 20723, USA

<sup>15</sup> Lunar and Planetary Laboratory, University of Arizona, 1629 East University Boulevard, Tucson, AZ 85721, USA

Received 2022 December 5; revised 2023 January 16; accepted 2023 January 17; published 2023 February 15

## Abstract

We report statistically significant detections of nonradial, nongravitational accelerations based on astrometric data in the photometrically inactive objects 1998 KY<sub>26</sub>, 2005 VL<sub>1</sub>, 2016 NJ<sub>33</sub>, 2010 VL<sub>65</sub>, 2016 RH<sub>120</sub>, and 2010 RF<sub>12</sub>. The magnitudes of the nongravitational accelerations are greater than those typically induced by the Yarkovsky effect, and there is no radiation-based, nonradial effect that can be so large. Therefore, we hypothesize that the accelerations are driven by outgassing and calculate implied H<sub>2</sub>O production rates for each object. We attempt to reconcile outgassing-induced acceleration with the lack of visible comae or photometric activity via the absence of surface dust and low levels of gas production. Although these objects are small, and some are rapidly rotating, the surface cohesive forces are stronger than the rotational forces, and rapid rotation alone cannot explain the lack of surface debris. It is possible that surface dust was removed previously, perhaps via outgassing activity that increased the rotation rates to their present-day value. We calculate dust production rates of order  $\sim 10^{-4}$  g s<sup>-1</sup> in each object, assuming that the nuclei are bare, within the upper limits of dust production from a sample stacked image of 1998 KY<sub>26</sub> of  $\dot{M}_{\text{dust}} < 0.2$  g s<sup>-1</sup>. This production corresponds to brightness variations of order  $\sim 0.0025\%$ , which are undetectable in extant photometric data. We assess the future observability of each of these targets and find that the orbit of 1998 KY<sub>26</sub>—which is also the target of the extended Hayabusa2 mission—exhibits favorable viewing geometry before 2025.

*Unified Astronomy Thesaurus concepts:* [Comae \(271\)](#); [Asteroids \(72\)](#)

## 1. Introduction

A typical—albeit simplistic—classification of solar system small bodies is to categorize the populations based on volatile-driven activity. In this classical picture, comets are defined as icy objects that produce dusty comae and presumably formed in distant regions of the solar system, while asteroids lack volatiles due to prolonged exposure to solar irradiation. However, recent advances have demonstrated that this simplistic classification may not be an accurate depiction of the census of small bodies within the solar system. A subset of objects on cometary orbits lack detectable activity, while some asteroids have displayed volatile-induced comae. These intriguing continuum objects could offer insights into little-

understood processes such as cometary fading (Brasser & Wang 2015) and volatile delivery to terrestrial planets (Chyba 1990; Owen & Bar-Nun 1995; Albarède 2009).

It is generally thought that asteroids can be grouped into classes based on their sizes. The typical timescale for an  $\sim 10$  km scale asteroid to experience a catastrophic impact is approximately the age of the solar system (Bottke et al. 2005, 2015). It is therefore believed that asteroids larger than  $\sim 10$  km are intact primordial remnants, while smaller objects with diameters between 200 m and  $\sim 10$  km are reaccumulated rubble piles held together by self-gravity (Harris 1979; Harris & Burns 1979; Harris 1996; Walsh 2018). As evidence, the  $\sim 17$  km equivalent diameter asteroid Eros visited by NEAR-Shoemaker displayed geologic properties consistent with being a damaged but intact primordial remnant (Cheng et al. 2002). Notable examples of extremely porous rubble-pile asteroids are (25143) Itokawa (Fujiwara et al. 2006), (162173) Ryugu (Watanabe et al. 2019), and (101955) Bennu (Barnouin et al. 2019).



Original content from this work may be used under the terms of the [Creative Commons Attribution 4.0 licence](#). Any further distribution of this work must maintain attribution to the author(s) and the title of the work, journal citation and DOI.

A subset of asteroids are known to exhibit activity, also called active asteroids (Jewitt 2012; Hsieh 2017; Jewitt & Hsieh 2022). Almost all active asteroids known to date have diameters consistent with being rubble piles, with the exception of the large objects (1) Ceres and (493) Griseldis. A subset of active asteroids are the main-belt comets (MBCs), objects that reside in the main asteroid belt between Mars and Jupiter and display cometary activity driven by the sublimation of volatiles (Hsieh & Jewitt 2006). The first MBC discovered was comet 133P/(7968) Elst–Pizarro (Boehnhardt et al. 1996; Elst et al. 1996; Toth 2000; Hsieh et al. 2004), and several others have since been identified: 238P/Read, 259P/Garradd, 288P/(300163) 2006 VW139, 313P/Gibbs, 324P/La Sagra, 358P/PANSTARRS, 107P/(4015) Wilson–Harrington, and 433P/(248370) 2005 QN173 (for images, see Figure 13 in Jewitt & Hsieh 2022).

Targeted, homogeneous searches for MBCs imply occurrence rates for these objects within the total population between  $<1/500$  and  $\sim 1/300$  (Bertini 2011; Sonnett et al. 2011; Snodgrass et al. 2017; Ferrellec et al. 2022). Indirect measurements of activity can come from anisotropic mass loss–driven nongravitational accelerations (Whipple 1950, 1951). For example, Hui & Jewitt (2017) reported statistically significant nongravitational accelerations in the active asteroids 313P/Gibbs, 324P/La Sagra, and (3200) Phaethon.

Nonsublimation effects such as impacts (Snodgrass et al. 2010) and rotational effects (Jewitt et al. 2014) can also cause activity in asteroids. The  $\sim 6$  km object (3200) Phaethon was first determined to be active when its association with the Geminid meteoroid stream was identified (Gustafson 1989; Williams & Wu 1993). Subsequent observations of (3200) Phaethon near its perihelion revealed a small tail with micron-sized dust production rates of  $\sim 3$  kg  $s^{-1}$  (Jewitt & Li 2010; Jewitt et al. 2013; Li & Jewitt 2013; Hui & Li 2017). Because these production rates are not large enough to explain the meteoroid stream, it has been suggested that processes such as repeated thermally induced stresses (Jewitt & Li 2010), sublimation of mineralogically bound sodium (Masiero et al. 2021), rotational effects (Ansdell et al. 2014; Nakano & Hirabayashi 2020), and geometric effects (Hanus et al. 2016; Taylor et al. 2019) also contribute to the activity of (3200) Phaethon. The Japan Aerospace Exploration Agency DESTINY+ mission will visit (3200) Phaethon and is expected to launch in 2024 (Arai et al. 2021). DESTINY+ will be equipped with a mass spectrometer that will detect elemental compositions of dust released by the object (Krüger et al. 2019).

Object (101955) Bennu is another intriguing case of an active asteroid. The OSIRIS-REx spacecraft observed repeated periods of particle ejection from the  $\sim 500$  m rubble pile (Hergenrother et al. 2019; Lauretta et al. 2019). The average mass-loss rate of dust was measured to be only  $\dot{M}_{\text{Dust}} \sim 10^{-4}$  g  $s^{-1}$  (Hergenrother et al. 2020), but the source of the activity is unclear (Bottke et al. 2020; Chesley et al. 2020; Molaro et al. 2020).

A somewhat related but distinct family of minor bodies are the inactive comets. For example, Manx comets are objects with long-period comet (LPC) trajectories that exhibit little or no cometary activity. The Manx comet C/2014 S3 (PANSTARRS) displayed levels of cometary activity that were 5–6 orders of magnitude less than typical comets and spectral features similar to S-type asteroids (Meech et al. 2016). The

origin of the Manx comets is unclear because Jupiter scatters objects within the  $H_2O$  snowline primarily into the interstellar medium and not into the Oort cloud (Hahn & Malhotra 1999; Shannon et al. 2015). Other inactive comets are Damocloids (named after the first object, (5335) Damocles; Asher et al. 1994; Jewitt 2005) and asteroids on cometary orbits (ACOs), defined as inactive objects on Halley-type or Jupiter-family comet (JFC) orbits, respectively. Damocloids and ACOs are believed to be comets that have little or no activity due to cometary fading (Wang & Brasser 2014; Brasser & Wang 2015) or the depletion of volatiles or mantling (Podolak & Herman 1985; Prialnik & Bar-Nun 1988). The observed spectral features and surface colors of Damocloids and ACOs indicate that they are likely extinct or dormant comets (Jewitt 2005; Licandro et al. 2018).

The recently discovered population of interstellar objects also appears to exhibit a continuum of apparent activity. The first interstellar object, 1I/‘Oumuamua, was detected on UT 2017 October 19 (Williams et al. 2017) and exhibited a mixture of cometary and asteroidal properties. On the other hand, the 0.2–0.5 km radius scale (Jewitt et al. 2020) 2I/Borisov displayed a visible cometary tail (Jewitt & Luu 2019; Bodewits et al. 2020; Cremonese et al. 2020; Guzik et al. 2020; Hui et al. 2020; Kim et al. 2020; Yang et al. 2021). The  $\sim 120$  m diameter 1I/‘Oumuamua displayed an extreme light-curve amplitude (Knight et al. 2017; Belton et al. 2018; Bolin et al. 2018; Drahus et al. 2018; Fraser et al. 2018; McNeill et al. 2018; Mashchenko 2019), reddened color (Bannister et al. 2017; Masiero 2017; Ye et al. 2017; Fitzsimmons et al. 2018), and incoming trajectory consistent with the local standard of rest (Gaidos et al. 2017; Mamajek 2017; Almeida-Fernandes & Rocha-Pinto 2018; Feng & Jones 2018; Hallatt & Wiegert 2020; Hsieh et al. 2021a). Of particular interest and relevance to this paper, ‘Oumuamua exhibited no evidence for an extended dust coma in deep stacked composite images (Jewitt et al. 2017; Meech et al. 2017). Moreover, it exhibited no obvious infrared fluorescence of carbon-based outgassing species (e.g., CO or  $CO_2$ ) based on observations obtained with the Spitzer Space Telescope (Trilling et al. 2018). However, the trajectory of the object was affected by a significant nongravitational acceleration (Micheli et al. 2018). Micheli et al. (2018) argued that the most likely cause of this acceleration—which was primarily in the radial direction opposite the direction of the Sun—was cometary outgassing. The physical properties of the first two interstellar interlopers are readily summarized; see Jewitt & Seligman (2022) and Moro-Martín (2022) for recent reviews.

Recently, Farnocchia et al. (2023) presented observations that revealed that the object 2003 RM exhibited a significant transverse nongravitational acceleration incompatible with the Yarkovsky effect. However, this object, like ‘Oumuamua, lacked cometary activity clearly visible in photometric images. They found that outgassing can cause the acceleration and still escape photometric detection. In this paper, we report the identification of similar nongravitational accelerations in five other small bodies on asteroid orbits.

## 2. Detections of Nongravitational Acceleration

### 2.1. Possible Nongravitational Perturbations on Small Bodies

The trajectories of small bodies are typically estimated from observational data sets, primarily optical astrometry and

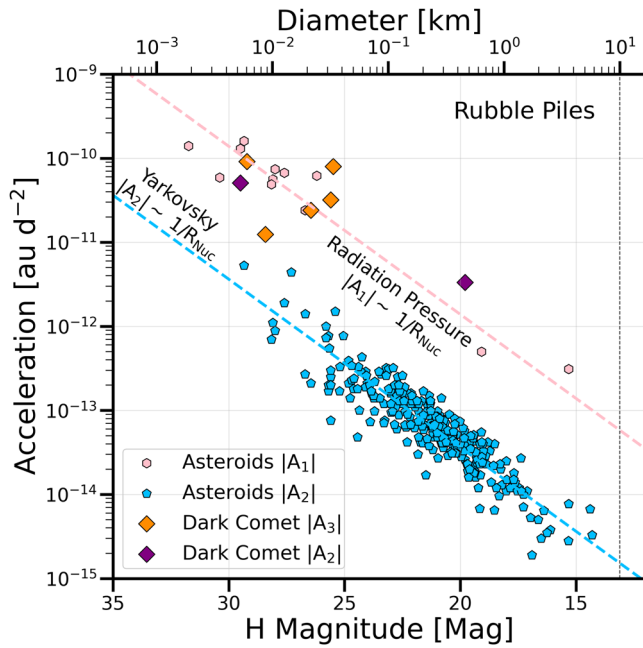


**Figure 1.** Nongravitational accelerations measured in asteroids vs. their absolute magnitude  $H$ . Measured radial nongravitational accelerations  $A_1$  are due to solar radiation pressure (pink), and transverse accelerations  $A_2$  are due to the Yarkovsky effect (blue). The out-of-plane nongravitational accelerations  $A_3$  measured in the objects presented in this paper are shown by orange diamonds. The blue and pink dashed lines show the lines of best fit, assuming that the acceleration is proportional to the inverse of the nuclear size and computed using the relationship in Equation (2), assuming an albedo of  $p = 0.1$ . The log-scaled intercepts are  $-15.858$  for the radiation pressure and  $-17.440$  for the Yarkovsky effect. The dark comet candidates with anomalous  $A_2$  values, 2003 RM and 2006 RH<sub>120</sub>, are shown by purple diamonds.

sometimes radar delay and Doppler measurements. As the observational arcs extend in time and the accuracy of the data improves, the resulting orbits become better constrained. Therefore, the requirements on the fidelity of the force model to compute the orbit become more stringent.

It has long been established that the motion of comets can be significantly perturbed by nongravitational accelerations due to outgassing, in addition to typical gravitational forces. Marsden et al. (1973) introduced a parametric model, where the nongravitational acceleration is described as

$$a_{\text{NG}} = (A_1 \hat{r} + A_2 \hat{t} + A_3 \hat{n}) g(r). \quad (1)$$

In Equation (1),  $\hat{r}$ ,  $\hat{t}$ , and  $\hat{n}$  are the orbital radial, transverse, and out-of-plane directions;  $g(r)$  is a function based on the H<sub>2</sub>O sublimation profile capturing the dependence on the heliocentric distance  $r$ ; and  $A_1$ ,  $A_2$ , and  $A_3$  are free parameters that give the acceleration components that the comet would experience at a heliocentric distance of  $r = 1$  au.

For asteroids, the two main nongravitational perturbations are the Yarkovsky effect (Vokrouhlický et al. 2015) and solar radiation pressure (Vokrouhlický & Milani 2000). By setting  $g(r) = (1 \text{ au}/r)^2$ , these two perturbations can be modeled as purely transverse  $A_2 g(r)$  and purely radial  $A_1 g(r)$  accelerations using the Marsden et al. (1973) formalism (e.g., Farnocchia et al. 2015). Despite being smaller than those on comets, these two perturbations can cause detectable deviations from a gravity-only trajectory for sufficiently long observational data arcs. In particular, the Yarkovsky effect has been detected on more than 200 near-Earth asteroids (e.g., Greenberg et al.

2020), shown by blue points in Figure 1. Solar radiation pressure is a radial acceleration and therefore less effective at producing significant orbital deviations. As such, it has been measured only on a handful of small asteroids (MPEC 2008-D12;<sup>16</sup> Micheli et al. 2012, 2013; Mommert et al. 2014a, 2014b; Micheli et al. 2014; Farnocchia et al. 2017; Fedorets et al. 2020), shown by pink points in Figure 1. As a testament to the fidelity of the modeling of the force model for asteroids, including these nongravitational forces, Farnocchia et al. (2021) were able to reconstruct the trajectory of asteroid (101955) Bennu by matching ground-based optical and radar astrometry from 1999 to 2018, as well as meter-level ranging measurements from the OSIRIS-REx mission proximity operations from 2019 January to 2020 October.

## 2.2. Asteroids with Excess Nongravitational Acceleration

In the accompanying paper (Farnocchia et al. 2023), we report the detection of an anomalously large nongravitational acceleration in the object 2003 RM. In that paper, we conclude that outgassing could have caused the acceleration of 2003 RM while not producing a detectable signature in photometric data. Further, Chesley et al. (2016) reported that the object 2006 RH<sub>120</sub>, which was temporarily captured by the Earth for about a year starting in 2006 June (Granvik et al. 2012), exhibited a transverse nongravitational acceleration that was inconsistent with the typical forces observed acting on asteroids. In this paper, we report the detection of out-of-plane nongravitational accelerations in a sample of five other objects that we measured from a combination of serendipitous (and uncoordinated) astrometric observations, 1998 KY<sub>26</sub>, 2005 VL<sub>1</sub>, 2016 NJ<sub>33</sub>, 2010 VL<sub>65</sub>, and 2010 RF<sub>12</sub>, all identified as point-source asteroidal objects with no extended dust coma or evidence for outgassing. We also detect significant out-of-plane perturbations for 2006 RH<sub>120</sub>. There have been no reports of clear detection of cometary activity for any of these small objects to the Minor Planet Center to date, and they are all classified as asteroids.

In 2020 December, we observed asteroid 1998 KY<sub>26</sub>—a potential Yarkovsky detection candidate (Vokrouhlický et al. 2000) and the target of the Hayabusa2 extended mission (Hirabayashi et al. 2021)—with the Very Large Telescope (VLT; MPEC 2020-X181)<sup>17</sup> with the purpose of improving the measurement of the orbit. At the same time, we also submitted two previously unreported observations from Maunakea in 2002 to the Minor Planet Center. While the Yarkovsky effect was included in the fit and detected, the VLT observations showed a  $-0''.2$  bias in decl. that was larger than the astrometric uncertainties. The bias was confirmed in additional observations from La Palma (MPEC 2021-A42)<sup>18</sup> and Maunakea (MPEC 2021-G127).<sup>19</sup> To ensure that the cause of this bias was not problematic data during the discovery apparition in 1998, we remeasured observations from the Modra Astronomical and Geophysical Observatory and Ondřejov, which, together with radar (Ostro et al. 1999), were the only observations from 1998 we included in the fit. Despite our data set revision, the bias still persisted. Adding solar radiation pressure through the  $A_1$  parameter was unfruitful, but

<sup>16</sup> <https://www.minorplanetcenter.net/mpec/K08/K08D12.html>

<sup>17</sup> <https://www.minorplanetcenter.net/mpec/K20/K20X11.html>

<sup>18</sup> <https://www.minorplanetcenter.net/mpec/K21/K21A42.html>

<sup>19</sup> <https://www.minorplanetcenter.net/mpec/K21/K21GC7.html>

adding an out-of-plane acceleration  $A_3(1 \text{ au}/r)^2$  removed the bias in the 2020 data.

Subsequently, we observed 2005 VL<sub>1</sub> in 2021 (MPEC 2021-X95)<sup>20</sup> and 2016 NJ<sub>33</sub> in 2022 (MPECs 2022-N88 and 2022-O09)<sup>21,22</sup> as Yarkovsky candidates. These observations were obtained with the 4.3 m Lowell Discovery Telescope in Arizona. Again, the collected data revealed a bias that could only be removed by adding an out-of-plane acceleration.

Another case arose when we noticed the similarity between the orbits of 2010 VL<sub>65</sub><sup>23</sup> and 2021 UA12.<sup>24</sup> The objects can be readily linked by fitting both data sets together, but only if  $A_3$  is estimated as part of the fit.

The last case is 2010 RF<sub>12</sub>, which we observed in 2022 from Maunakea with the Canada–France–Hawaii Telescope and from Cerro Paranal with the VLT with the purpose of ruling out impact solutions detected by impact monitoring systems such as Sentry<sup>25</sup> and ESA’s own system.<sup>26</sup> The observations we collected, in combination with an archival Maunakea set of images from 2011 taken with the Subaru Telescope (MPEC 2022-S77),<sup>27</sup> once again revealed a bias that could only be removed by estimating  $A_3$  while fitting the data.

Given these results, we decided to review the fit for 2006 RH<sub>120</sub> and found that in that case, there is also significant detection of an out-of-plane acceleration in addition to the radial and transverse ones.

In Table 1, we list each component,  $A_1$ ,  $A_2$ , and  $A_3$ , of the best-fit nongravitational accelerations and their associated uncertainties. In order to avoid underestimating the uncertainty in the  $A_1$ ,  $A_2$ , and  $A_3$  parameters, we estimate all three parameters even when some of them (especially  $A_1$ ) are not significantly detected. For each of these fits, we adopt  $g(r) = (1 \text{ au}/r)^2$ . As examples, we show the R.A. and decl. residuals of the astrometric fits with and without nongravitational accelerations for 2010 VL<sub>65</sub> and 2005 VL<sub>1</sub> in Figure 2. The improvement in the fit is evident from the figure. For VL<sub>65</sub>, the gravity-only fit results in residuals as large as  $10''$ . For 2005 VL<sub>1</sub>, it is clear how the bias in 2021 (but also systematic errors in 2005) is removed by adding nongravitational accelerations.

In Figure 1, we show the best-fit  $A_2$  and  $A_3$  parameters for the nonradial, nongravitational acceleration for each object. We compare the estimated  $A_2$  and  $A_3$  to the measured nongravitational accelerations in asteroids. We show both  $A_1$ , which is related to solar radiation pressure, and  $A_2$ , which is related to the Yarkovsky effect. Computed fits of the acceleration, being inversely proportional to the nuclear radius computed using Equation (2), are shown. There is a linear correlation between  $\log|A_2|$  and  $H$  (blue dashed line), as is expected from the Yarkovsky relation (Vokrouhlický et al. 2015). The scatter around the mean is presumably due to different albedo, density, obliquity, or surface thermal inertia values. As a rule of thumb,  $\log|A_1|$  versus  $H$  (pink dashed line) again shows a linear trend with the same slope but an approximately order-of-magnitude larger normalization (Vokrouhlický & Milani 2000). The nonradial component of the detected accelerations appears to

be more consistent with the extrapolation of the  $A_1$  values. However, solar radiation pressure is mostly radial, and only a minor fraction would project in the out-of-plane direction (Vokrouhlický & Milani 2000). Specifically, Vokrouhlický & Milani (2000) demonstrated that small off-radial components of nongravitational accelerations could emerge from radiation pressure because of variable albedo or nonspherical shapes. This suggests that these accelerations are inconsistent with radiation effects.

Based on this analysis, we conclude that there are significant out-of-plane accelerations for all of these objects. If the out-of-plane accelerations in these objects are in fact caused by outgassing, it is possible that these are manifestations of nearly polar jets with spin axes orthogonal to the orbit plane.

The radial  $A_1$  values are all consistent with zero acceleration, with the possible exception of 2016 NJ<sub>33</sub>. Moreover, the  $A_2$  values are much smaller in magnitude than the  $A_3$  values and generally consistent with the Yarkovsky effect. In the case of 2003 RM and 2006 RH<sub>120</sub>, the  $A_2$  values are anomalously high and presumably due to outgassing (Chesley et al. 2016). Therefore, in the rest of the paper, we focus on  $A_3$  only. We note, however, that if high-latitude jets are in fact causing the nongravitational accelerations, this would be somewhat distinct from typical comets that exhibit outgassing events isotropically over their surfaces. Moreover, incident stellar irradiation and subsequent surface temperature variations should not only affect the out-of-plane acceleration. This analysis could be generalized to larger accelerations if  $A_1$  were to be statistically detected with longer data arcs.

Table 1 summarizes the observed orbital properties, absolute magnitudes, and rotational periods (where measured) for each of these objects. We use the following equation (Pravec & Harris 2007) to estimate the sizes for all objects except 1998 KY<sub>26</sub>, 2003 RM, and 2006 RH<sub>120</sub>:

$$2R_{\text{Nuc}} = \left( \frac{1329}{\sqrt{p}} \right) 10^{-0.2H}, \quad (2)$$

where  $H$  is the absolute magnitude,  $p$  is the geometric albedo, and  $R_{\text{Nuc}}$  is the radius in kilometers. In Table 1, we assume  $p = 0.1$  to estimate the size of objects where this value has not been previously measured. The trajectories of the objects are unremarkable. In Figure 3, we show the location of these candidate “dark comets,” as well as the location of all of the currently known active asteroids, whose properties are listed in Table 3.

### 2.3. Lack of Cometary Activity Detection

None of the objects studied in this paper have reported cometary activity. Out of all of our candidate targets, 1998 KY<sub>26</sub> was the only one for which we had meaningful data that could provide limits on the dust production. The 1998 KY<sub>26</sub> images were obtained using Unit Telescope 1 of the ESO VLT on Mount Paranal, Chile, with FORS2 (Appenzeller et al. 1998). The instrument was used without a filter (white light) in order to reach the deepest possible limiting magnitude on asteroids and dust. FORS2 was equipped with a mosaic of two MIT/LL CCD detectors, of which only the main chip, A, or CCID20-14-5-3, was used. The CCD was read with  $2 \times 2$  binning, resulting in  $0''.252$  on sky. The debiased and flat-fielded images were aligned on the position of the target. In Figure 4, we show a stack of the images from 2020 December

<sup>20</sup> <https://www.minorplanetcenter.net/mpec/K21/K21X95.html>

<sup>21</sup> <https://www.minorplanetcenter.net/mpec/K22/K22N88.html>

<sup>22</sup> <https://www.minorplanetcenter.net/mpec/K22/K22O09.html>

<sup>23</sup> [https://ssd.jpl.nasa.gov/tools/sbdb\\_lookup.html#/?sstr=2010v165](https://ssd.jpl.nasa.gov/tools/sbdb_lookup.html#/?sstr=2010v165)

<sup>24</sup> [https://ssd.jpl.nasa.gov/tools/sbdb\\_lookup.html#/?sstr=2021ua12](https://ssd.jpl.nasa.gov/tools/sbdb_lookup.html#/?sstr=2021ua12)

<sup>25</sup> <https://cneos.jpl.nasa.gov/sentry/>

<sup>26</sup> <https://neo.ssa.esa.int/risk-list>

<sup>27</sup> <https://www.minorplanetcenter.net/mpec/K22/K22S77.html>

**Table 1**  
Objects with Anomalous Nongravitational Accelerations

Object	$a$ (au)	$e$	$i$ (deg)	$q$ (au)	$H$ (mag)	$R_{\text{Nuc}}$ (m)	$P_{\text{Rot}}$ (hr)	$A_1$ ( $10^{-10}$ au day $^{-2}$ )	Signif. ( $\sigma$ )	$A_2$ ( $10^{-10}$ au day $^{-2}$ )	Signif. ( $\sigma$ )	$A_3$ ( $10^{-10}$ au day $^{-2}$ )	Signif. ( $\sigma$ )	$Q(\text{H}_2\text{O})$ ( $10^{20}$ molecules s $^{-1}$ )
1998 KY <sub>26</sub>	1.23	0.20	1.48	0.98	25.60	15	0.178	$1.73 \pm 0.91$	2	$-0.00126 \pm 0.00061$	2	$0.320 \pm 0.115$	3	9.19
2005 VL <sub>1</sub>	0.89	0.23	0.25	0.69	26.45	11		$-6.66 \pm 8.02$	<1	$-0.00711 \pm 0.00592$	1	$-0.240 \pm 0.041$	6	5.5
2016 NJ <sub>33</sub>	1.31	0.21	6.64	1.04	25.49	16	0.41-1.99	$9.28 \pm 2.96$	3	$-0.00566 \pm 0.00193$	3	$0.848 \pm 0.163$	5	24.8
2010 VL <sub>65</sub>	1.07	0.14	4.41	0.91	29.22	3		$6.57 \pm 13.0$	<1	$-0.00146 \pm 0.00534$	<1	$-0.913 \pm 0.130$	7	0.24
2010 RF <sub>12</sub>	1.06	0.19	0.88	0.86	28.42	4		$0.488 \pm 0.597$	<1	$-0.00136 \pm 0.00286$	<1	$-0.168 \pm 0.021$	8	0.12
2006 RH <sub>120</sub>	1.00	0.04	0.31	0.96	29.50	2-7	0.046	$1.38 \pm 0.08$	18	$-0.507 \pm 0.0637$	8	$-0.130 \pm 0.032$	4	1.5
2003 RM	2.92	0.60	10.86	1.17	19.80	230		$-1.045 \pm 1.217$	<1	$0.0215 \pm 0.0004$	56	$0.0156 \pm 0.0543$	<1	1600

**Note.** Best-fit nongravitational acceleration parameters for each object in our sample, with formal ( $1\sigma$ ) uncertainties. The statistical significance is given for each acceleration and calculated as the ratio of the magnitude of the acceleration to its uncertainty. We also include the object 2003 RM, for which we report anomalously large nongravitational acceleration in the accompanying paper (Farnocchia et al. submitted 2022). Statistically robust results ( $\sigma \geq 3$ ) are found for the  $A_3$  component of all newly reported objects in this paper. For the  $A_2$  component, only 2016 NJ<sub>33</sub>, 2003 RM, and 2006 RH<sub>120</sub> have robust detections. We calculate implied production rates of H<sub>2</sub>O for each object in our sample at perihelion. We calculate this using the most significant component of the acceleration and assuming an albedo of  $p = 0.1$  and that the molecules are released at a temperature of 100 K. The size and rotational period of 1998 KY<sub>26</sub> were first reported by Ostro et al. (1999). The rotational period of 2016 NJ<sub>33</sub> is estimated from radar CW spectral observations taken with the Arecibo Observatory planetary radar system (see Appendix A). The nuclear radius and period of 2006 RH<sub>120</sub> were reported by Kwiatkowski et al. (2009). The remaining objects do not have reported measurements of size or rotational period. We estimate the remaining sizes with Equation (2) assuming a geometric albedo of  $p = 0.1$ .

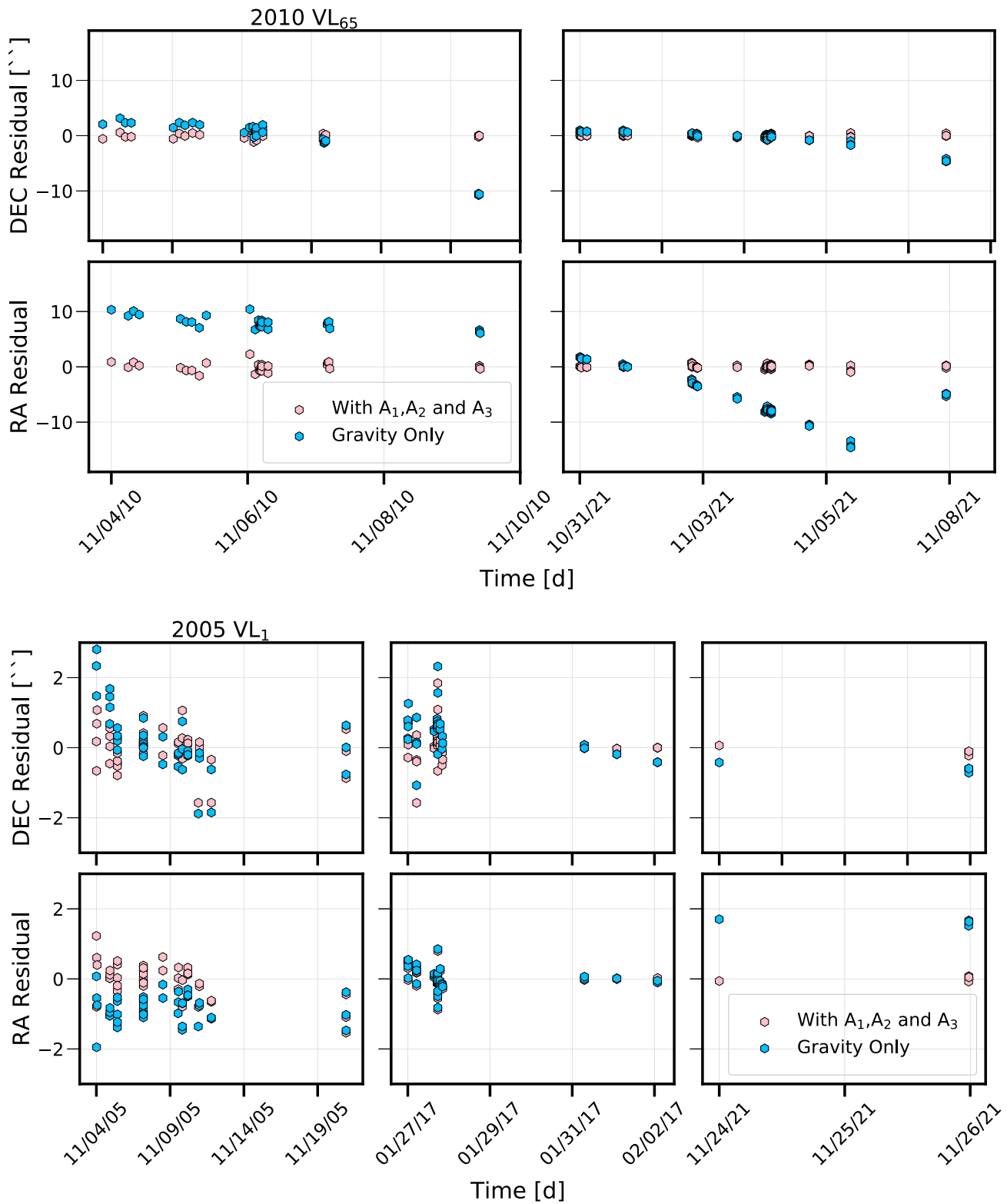


**Figure 2.** The (signed) residuals of the astrometric fits (in arcseconds) for the R.A. and decl. of 2010 VL<sub>65</sub> (top) and 2005 VL<sub>1</sub> (bottom) with (pink points) and without (blue points) nongravitational accelerations. The gravity-only solution does not allow for outlier rejection in the astrometric fits.

where no background object was too close to the object. This image contains 120 exposures of 30 s each, resulting in a 3600 s exposure.

The object was rather faint (26.1 for the first set, 25.5 for the second), requiring that the astrometric measurements be performed on stacks. The signal-to-noise ratio (S/N) in the

individual images is barely above 1. This implies that the photometry would also require stacks. The object is the blob at the center, outlined with a red circle. Although the object is very faint, the stacked images produce a solid detection with a combined S/N  $\sim 12$ . Furthermore, 1998 KY<sub>26</sub> is clearly visible in various substacks, confirming without doubt the reality of

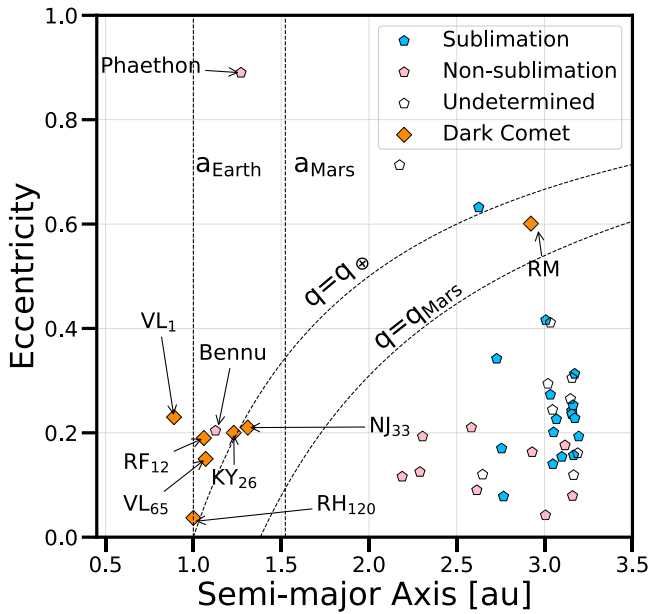


**Figure 3.** Location in semimajor axis and eccentricity space of the currently known active asteroids (pentagons; Table 3) and candidate dark comets (diamonds; Table 1). Active asteroids are color coded based on their activity sources: sublimation-driven activity (blue), nonsublimation-driven activity (pink), and unknown activity source (white). The semimajor axes of Mars and the Earth and orbits with perihelia equal to those of Mars and the Earth are indicated with dashed lines.

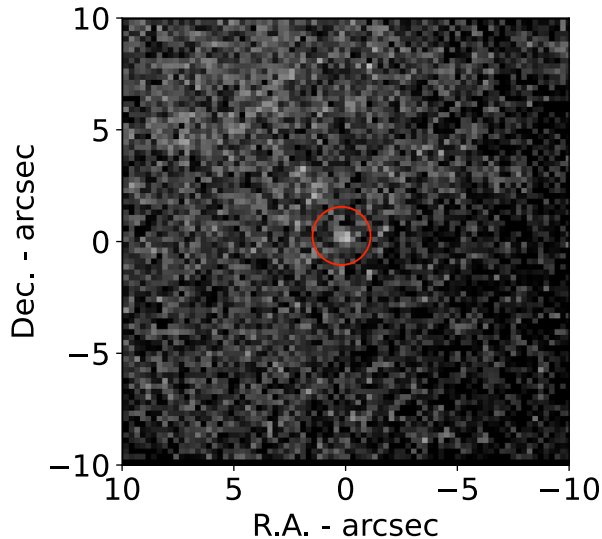


**Figure 4.** Stacked and cleaned image of 1998 KY<sub>26</sub> with VLT that spans two sets of 60 exposures, each of which is 30 s. The resulting temporal coverage is  $\sim 1$  hr in 2020 December. The image is  $64'' \times 64''$ . This is a linear gray scale from 0 to 4 ADU  $s^{-1}$  pixel $^{-1}$ . Object 1998 KY<sub>26</sub> is faint but visible in the final image and indicated with a red circle. There is no evidence for an extended cometary tail.

the image and its identification with the object (the image is  $64'' \times 64''$ ). There is no evidence for an extended tail in the deep image; the variations observed in the sky around the object can be identified with the residuals of the various background objects passing behind the object. In order to further quantify the lack of dust around the target, we show its photometric profile in Figure 5.

The selection of the images composing the stack used to generate the profile ensured that no background object

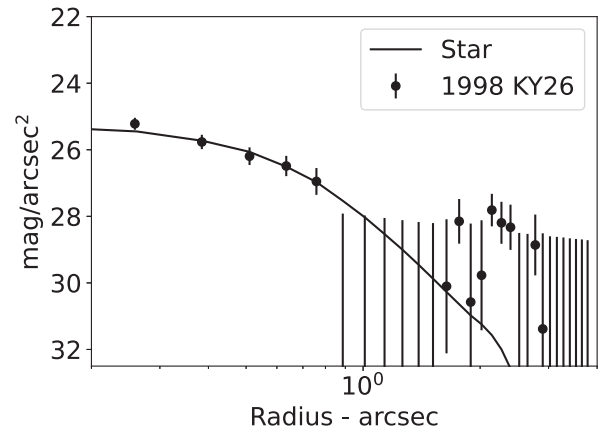


**Figure 5.** Standard profile analysis for dust activity in the deep stacked and cleaned image with VLT of 1998 KY<sub>26</sub> shown in Figure 4. The upper limit of dust present in the image is  $\sim 3$  kg. The solid line indicates the profile of our chosen field star scaled to the brightness of the object. The filled points indicate the integrated flux in concentric rings centered on the target. This analysis assumes that the dust is composed of  $1 \mu m$  sized dust grains with an albedo of  $p = 0.2$  and density of  $\rho = 3000 \text{ kg m}^{-3}$  with  $\sim 1$  order of magnitude uncertainty. The  $x$ -axis increases to the right.

would contaminate the area of the profile. We obtained it by integrating the instrumental fluxes converted to surface brightnesses in a set of concentric circular apertures centered on the object. We use a conversion to magnitudes with a zero-point of 27.8 (from Hainaut et al. 2021). To scale the brightness of the object for comparison, we used the profile of a field star. This analysis does not yield a stringent constraint because the noise and background dominate very quickly. Because this object is so faint, the quantity of dust that could be undetected in the image is not well constrained. We estimate a coma mass upper limit of  $\sim 3$  kg of dust by integrating the corresponding flux from  $0''.5$  to  $2''$  (assuming  $1 \mu m$  sized dust grains with an albedo of  $p = 0.2$  and density of  $\rho = 3000 \text{ kg m}^{-3}$ ). This corresponds to a magnitude for the dust of 24.0, which would be a  $5\sigma$  detection from  $0''.5$  to  $2''$  from the object. The uncertainty is  $\sim 1$  order of magnitude because of all the assumptions required to convert from the magnitudes to the mass of dust (grain size, albedo, and density). The corresponding upper limit on the dust production rate is  $\dot{M}_{\text{Dust}} < 0.2 \text{ g s}^{-1}$ . However, as discussed in the next section, outgassing could still explain the acceleration even if the upper limit was orders of magnitude higher.

### 3. Implied Production Rates

Based on the results presented in the previous section, it is clear that no mass loss has been detected in any of these dark comet candidates. However, the magnitudes of the nongravitational accelerations are inconsistent with being caused by the Yarkovsky effect or radiation pressure. Therefore, for the remainder of this paper, we hypothesize that the nonradial, nongravitational accelerations are caused by outgassing. We calculate the implied production rates of  $H_2O$  using only the dominant, nonradial accelerations.

The production rate  $Q(X)$  for a given species denoted by  $X$  may be calculated using

$$Q(X) = \left( \frac{M_{\text{Nuc}}}{m_X} \right) \left( \frac{|A_i|}{v_{\text{Gas}} \zeta} \right). \quad (3)$$

In Equation (3),  $M_{\text{Nuc}}$  is the mass of the nucleus,  $m_X$  and  $v_{\text{Gas}}$  are the mass and velocity of the outgassing species, and  $A_i$  is the dominant component of the nongravitational acceleration used in the calculation. The variable  $\zeta$  indicates the isotropy of the outflow, where  $\zeta = 1$  corresponds to a collimated outflow, and  $\zeta = 0.5$  corresponds to an isotropic hemispherical outflow. The velocity of the gas can be related to the temperature of the outflow,  $T_{\text{Gas}}$ , using

$$v_{\text{Gas}} = \left( \frac{8k_B T_{\text{Gas}}}{\pi m_X} \right)^{1/2}. \quad (4)$$

We calculate the implied production rates of  $\text{H}_2\text{O}$  outgassing using Equations (3) and (4) at perihelion (Table 1). We assume that  $\zeta = 1$  and that the nuclei of the objects are spherical with radii listed in Table 1, which in turn are calculated assuming an albedo of 0.1 and a bulk density of  $\rho_{\text{Bulk}} = 1 \text{ g cm}^{-3}$ . These production rates,  $\sim 10^{21}$  molecules  $\text{s}^{-1}$ , are several orders of magnitude lower than typical cometary production rates, which are on the order of  $\sim 10^{26}$  molecules  $\text{s}^{-1}$  (see Tables 1–3 in Harrington-Pinto et al. 2022). The implied mass production of  $\text{H}_2\text{O}$  of 1998 KY<sub>26</sub> is  $\sim 0.03 \text{ g s}^{-1}$ , compared to  $\lesssim 1 \text{ kg s}^{-1}$  for MBCs and  $\sim 10^2\text{--}10^3 \text{ kg s}^{-1}$  for comets (Jewitt 2012; Jewitt & Hsieh 2022). If 1998 KY<sub>26</sub> has been outgassing continuously at this rate since its discovery, the total mass lost would be  $\sim 10^7 \text{ g}$ ,  $\sim 0.1\%$  of its total mass. The analogous calculations for the other dark comet candidates yield similarly small mass-loss fractions, implying that outgassing is an allowable mechanism. The production of MBCs has not led to detectable gas production (Snodgrass et al. 2017), except for a tentative detection of one candidate by Ferellec et al. (2022).

It should be noted that the case of 2016 NJ<sub>33</sub> requires an  $\sim 3\sigma$  significant  $A_1$  radial acceleration to fit the astrometric data. We calculate the implied production rate using only the  $A_3$  acceleration. However, if  $A_1$  is as large as the fit suggests, then the implied production of  $\text{H}_2\text{O}$  would be slightly higher.

The characteristic mass-loss timescale  $\tau_M$  for which this level of activity is sustainable is approximately given by

$$\tau_M \simeq M_{\text{Nuc}} / \left( \frac{dM_{\text{Nuc}}}{dt} \right) \simeq \left( \frac{v_{\text{Gas}} \zeta}{|A_i|} \right). \quad (5)$$

A scaled relationship version of Equation (5) gives

$$\tau_M = 2.8 \times 10^4 \text{ yr} \left( \frac{v_{\text{Gas}}}{350 \text{ m s}^{-1}} \right) \left( \frac{2 \times 10^{-11} \text{ au day}^{-2}}{|A_i|} \right). \quad (6)$$

The orbits in our sample are similar to those of typical evolved near-Earth objects and may have had long residency times. From Equation (6), it is evident that these objects could not have been outgassing at these inferred rates for longer than  $\sim 10^4 \text{ yr}$ . Therefore, if these objects are outgassing, they either (i) were not outgassing at this rate in the recent past or (ii) were only recently emplaced on these orbits. Objects with trajectories similar to those of our sample dark comet candidates are thought to evolve from the main belt. Specifically, there is currently no known dynamical pathway to inject these objects from the JFC or LPC populations (see, e.g., Figures 4–6 in Granvik et al. 2018). Moreover, these objects all have the highest probability of being injected onto their current trajectories from the  $\nu_6$  region in the innermost part of the asteroid belt. If our interpretation of the

nongravitational acceleration based on outgassing is correct, it might have interesting population-wise implications for very small objects in the inner main belt. Although outside of the scope of this paper, future investigation of the dynamical history of these objects would be informative.

## 4. Possible Explanation for Lack of Visible Comae

### 4.1. Cohesive versus Rotational Forces for Surface Dust Retention

The objects in our sample are between  $\sim 3$  and  $15 \text{ m}$  in radius, smaller than typical cometary nuclei that have been measured (Jewitt & Seligman 2022). Because small objects tend to rotate faster, surface dust will experience stronger rotational forces. However, when considering typical cohesive forces on the surface regoliths of asteroids, it is evident that the rapid rotation of these objects is not sufficient to explain the lack of comae.

Consider a particle at the equator and on the surface of a spherical nucleus with a radius  $R_{\text{Nuc}}$  and a uniform density  $\rho_{\text{Bulk}}$ . In the absence of cohesive surface forces, the particle will be removed if its velocity is greater than the escape velocity,  $v_{\text{Esc}}$ , which is given by

$$v_{\text{Esc}} = R_{\text{Nuc}} \sqrt{\frac{8\pi}{3} G \rho_{\text{Bulk}}}. \quad (7)$$

A scaled version of the same equation gives the following relationship:

$$v_{\text{Esc}} = 7.48 \text{ cm s}^{-1} \left( \frac{R_{\text{Nuc}}}{1 \text{ km}} \right) \left( \frac{\rho_{\text{Bulk}}}{1.0 \text{ g cm}^{-3}} \right)^{1/2}. \quad (8)$$

The rotational velocity  $v_{\text{Rot}}$  at the surface of a spherical nucleus rotating with a rotational period  $P_{\text{Rot}}$  is  $v_{\text{Rot}} = 2\pi R_{\text{Nuc}} / P_{\text{Rot}}$ . If the rotational velocity is greater than the escape velocity—if  $v_{\text{Rot}} > v_{\text{Esc}}$ —then cohesionless particles will not remain on the surface. It is critical to note that this criterion only holds at the equator and is diminished at higher latitudes. This criterion reduces to the following expression:

$$P_{\text{Rot}} < \sqrt{\frac{3\pi}{2 G \rho_{\text{Bulk}}}}. \quad (9)$$

The critical rotational period,  $P_{\text{Crit}}$ —analogous to the rotation limit for a cohesionless rubble-pile object (Harris 1979; Harris & Burns 1979; Harris 1996; Warner et al. 2009)—is given by

$$P_{\text{Crit}} = 2.33 \text{ hr} \left( \frac{1 \text{ g cm}^{-3}}{\rho_{\text{Bulk}}} \right)^{1/2}. \quad (10)$$

If an object has a rotational period less than the critical period,  $P_{\text{Rot}} < P_{\text{Crit}}$ , particles without cohesive forces will not be retained on the surface. It has been established that the rotation periods of comets (when measured) are slower than those of asteroids (Binzel et al. 1992; Jewitt 2021; Jewitt & Hsieh 2022). In Figure 6, we show the rotational period versus perihelion for all comets for which the rotational period of the nucleus has been measured. The comets all have slow nuclear rotational periods and therefore weak rotational forces operating on their surfaces. Clearly, 1998 KY<sub>26</sub>, 2006 RH<sub>120</sub>, and 2016 NJ<sub>33</sub> are rotating faster than this critical period. The comet data shown in



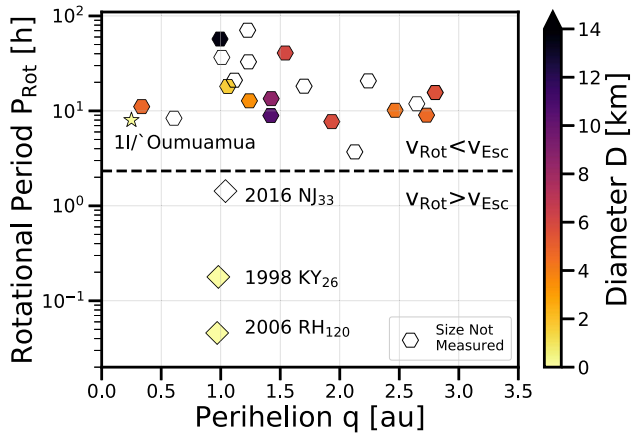


**Figure 6.** Nuclear rotational periods of comets for which this values has been measured vs. their perihelia. The nuclear diameter is shown in color for objects where this quantity has been measured. The locations of 1998 KY<sub>26</sub>, 2006 RH<sub>120</sub>, and 11/'Oumuamua are indicated, as well as the upper estimated rotation period of 2016 NJ<sub>33</sub>. The dashed line shows the critical rotation period where self-gravity balances with rotational forces. The data for each comet are listed in Table 2.

Figure 6 are listed in Table 2, with references for the cometary rotation period measurements.

However, it is worth noting that smaller dust may be retained on the surface by cohesion given by molecular forces or some electrostatic interaction (Rozitis et al. 2014). In fact—and somewhat counterintuitively—smaller objects tend to have more dominant cohesive forces (Scheeres et al. 2010; Sánchez & Scheeres 2020). The rotational force acting on the equatorial particle is  $f_{\text{Rot}} = m_{\text{D}} R_{\text{Nuc}} \omega_{\text{Nuc}}$  (where  $\omega_{\text{Nuc}}$  is the rotational frequency of the comet nucleus, and  $m_{\text{D}}$  is the mass of the dust grain). The cohesive forces can be estimated as  $f_{\text{Coh}} = \sigma_{\text{C}} \Delta A_{\text{D}}$ , where  $\sigma_{\text{C}}$  is the strength of the regolith, and  $\Delta A_{\text{D}}$  is the surface area of the grain (as in Section 2 of Sánchez & Scheeres 2020). Typical values of  $\sigma_{\text{C}}$  are  $\sim 0$ –100 Pa (Hirabayashi et al. 2014). Ignoring the effects of self-gravity, the cohesive forces will dominate over the rotational forces when the fraction  $f_{\text{Coh}} > f_{\text{Rot}}$ . Assuming that  $m_{\text{D}} \simeq \rho_{\text{D}} R_{\text{D}}^3$  and  $\Delta A_{\text{D}} \simeq R_{\text{D}}^2$  for grain size  $R_{\text{D}}$  and density  $\rho_{\text{D}}$ , the ratio of cohesive to rotational forces can be written as

$$\frac{f_{\text{Coh}}}{f_{\text{Rot}}} = 3283 \left( \frac{\sigma_{\text{C}}}{10 \text{ Pa}} \right) \left( \frac{1 \text{ g cm}^{-3}}{\rho_{\text{D}}} \right) \times \left( \frac{1 \text{ mm}}{R_{\text{D}}} \right) \left( \frac{1 \text{ km}}{R_{\text{Nuc}}} \right) \left( \frac{P_{\text{Rot}}}{1 \text{ hr}} \right)^2. \quad (11)$$

In Figure 7, we show a two-dimensional histogram of the diameter and rotational period of all asteroids for which these properties have been measured. The diameter ranges for which asteroids are believed to be rubble piles and primordial remnants as outlined in Walsh (2018) are indicated. We also show the location of all of the currently known active asteroids. It is evident that 1998 KY<sub>26</sub> and 2016 NJ<sub>23</sub>—and presumably the remaining candidate dark comets—are distinct at the population level from active and inactive asteroids. The dashed line shows the critical rotation period given by Equation (10), and the dotted line shows where the cohesive forces equal the rotational forces computed with Equation (11), assuming millimeter-sized dust grains,  $\sigma_{\text{C}} = 10 \text{ Pa}$ , and  $\rho_{\text{D}} = 1 \text{ g cm}^{-3}$ . It is clear that although the candidate dark comets rotate rapidly, typical cohesive forces will retain dust regolith on the

surface. Therefore, the rapid rotation periods alone cannot explain the lack of detectable dust activity for these objects.

#### 4.2. Dependence of Spin-up Timescale on Object Size

It is straightforward to show that, for a given sublimation torque, smaller objects spin up faster (the same holds for the radiation-induced torques, aka the YORP effect, which are, however, less important in the case of our sample of objects). Again, we consider a spherical nucleus with radius  $R_{\text{Nuc}}$ . If the outgassing induces average anisotropic rotational forces on the nucleus,  $F_{\text{Gas}}$ , the resulting torque is  $\vec{\tau}_{\text{Gas}}$ ,

$$\vec{\tau}_{\text{Gas}} \sim R_{\text{Nuc}} \times F_{\text{Gas}}. \quad (12)$$

This torque produces a change of rotational frequency of the comet nucleus,  $\dot{\omega}_{\text{Nuc}}$ ,

$$\vec{\tau}_{\text{Gas}} \sim M_{\text{Nuc}} R_{\text{Nuc}}^2 \frac{d\vec{\omega}_{\text{Nuc}}}{dt}. \quad (13)$$

By combining the previous two equations, the rate of change of the spin of the nucleus is given by (neglecting the  $\sin(\theta)$  term from the cross product)

$$\frac{d\omega_{\text{Nuc}}}{dt} \propto \frac{|F_{\text{Gas}}|}{M_{\text{Nuc}} R_{\text{Nuc}}}. \quad (14)$$

And, although this is a very general argument, surface forces on small bodies should be proportional to the surface area, i.e.,  $F_{\text{Gas}} \propto R_{\text{Nuc}}^2$ . Thus, for a given bulk density, we obtain

$$\frac{d\omega_{\text{Nuc}}}{dt} \propto \frac{1}{R_{\text{Nuc}}^2}. \quad (15)$$

Therefore, smaller objects will be particularly susceptible to rapid spin-up from outgassing torques. In Figure 7, the most rapidly rotating objects are preferentially small ( $\lesssim 1 \text{ km}$ ) in diameter. It is important to note, however, that the magnitude of outgassing torques scales with the production, which could depend on the size of the nucleus with a different power than the two assumed here. Based on the ratio of cohesive to rotational forces, it is possible that the rapid rotation of these small objects contributed to the removal of dust if the objects were spun up via outgassing and that same outgassing removed dust previously. However, the rotational forces alone, even for these rapidly rotating objects, are not sufficiently strong to remove surface dust.

#### 4.3. Subsurface Dust Production

Given that our candidate dark comets do not exhibit dust comae, if their accelerations are caused by outgassing, they must not have retained significant dust on their surfaces. It is not clear what mechanism removed the dust from the surface of the nuclei, given that rotation is not sufficient to overcome typical cohesive forces. It is possible that previous outgassing activity removed surface dust, and that the preferential rapid rotation in these dark comets is a leftover signature of this process. Processes such as meteorite bombardment (as with (101955) Bennu) and fatigue due to thermal cycling will replenish surface dust, so for the nuclei to remain bare, the removal rate of dust via outgassing must be larger than the generation rate. Moreover, the episodic nature of these mechanisms militates against detection. It is also possible that significant surface material was cleared rapidly at birth, and the

**Table 2**  
Comets with Nuclear Rotation Periods Measured

Object Name	$q$ (au)	$i$ (deg)	Classification	Diameter (km)	$P_{\text{Rot}}$ (hr)	Reference
P/2006 HR30 (Siding Spring)	1.226	31.88	HTC		70.7	
C/2001 OG108 (LONEOS)	0.994	80.25	HTC	13.6	57.12	Abell et al. (2005)
9P/Tempel 1	1.542	10.47	JFC	6	40.7	Fernández et al. (2005a) A'Hearn et al. (2005)
P/2016 BA14 (PANSTARRS)	1.009	18.92	JFC		36.6	Warner (2016)
162P/Siding Spring	1.233	27.82	JFC		32.853	Kokotanekova et al. (2017)
333P/LINEAR	1.115	131.88	JFC		21.04	Hicks & Thackeray (2016)
94P/Russell 4	2.24	6.18	ETC		20.7	Kokotanekova et al. (2017)
93P/Lovas 1	1.7	12.2	JFC		18.2	Kokotanekova et al. (2017)
103P/Hartley 2	1.059	13.62	JFC	1.6	18.1	Belton et al. (2013) Harmon et al. (2011)
47P/Ashbrook–Jackson	2.802	13.05	JFC	5.6	15.6	Kokotanekova et al. (2017)
49P/Arend–Rigaux	1.424	19.05	JFC	8.48	13.45	Eisner et al. (2017)
67P/Churyumov–Gerasimenko	1.241	7.05	JFC	3.4	12.761 29	Mottola et al. (2014) Sierks et al. (2015)
149P/Mueller 4	2.647	29.75	JFC		11.88	Kokotanekova et al. (2017)
2P/Encke	0.336	11.78	ETC	4.8	11.083	Fernández et al. (2005b) Lowry & Weissman (2007)
110P/Hartley 3	2.465	11.7	JFC	4.3	10.153	Kokotanekova et al. (2017)
14P/Wolf	2.729	27.94	JFC	4.66	9.02	Kokotanekova et al. (2017)
10P/Tempel 2	1.421	12.03	JFC	10.6	8.93	A'Hearn et al. (1989) Jewitt & Luu (1989) Wisniewski (1990) Knight et al. (2012)
169P/NEAT	0.607	11.3	JFC		8.369	
137P/Shoemaker–Levy2	1.933	4.85	JFC	5.8	7.7	Kokotanekova et al. (2017)
123P/West–Hartley	2.126	15.35	JFC		3.7	Kokotanekova et al. (2017)
C/2003 WT42 (LINEAR)	5.191	31.41	HYP		3.31	Dermawan et al. (2011)

**Note.** The data are drawn from the JPL small-body database.

present-day dust creation rate is low enough to avoid apparent comae detection.

If these small objects are unable to retain surface material, the only possible source of dust activity is from subsurface dust, which is entrained during ice sublimation. Assuming the nongravitational acceleration is due to volatile outgassing, we calculate the maximum amount of dust that could be produced via such entrainment, assuming the dust-to-gas mass ratio  $\mathcal{Z} = 0.01$  typically assumed in the interstellar medium and protoplanetary disks (Birnstiel et al. 2010). The dust production rate  $\dot{M}_{\text{Dust}}$  for a given outgassing species  $X$  can be calculated from the gas production rate (Table 1) by multiplying the total gas mass production of the outflow by the dust-to-gas ratio. Assuming  $\text{H}_2\text{O}$ -driven gas production, the dust production can be calculated using

$$\dot{M}_{\text{Dust}}(X) = 3 \times 10^{-4} \text{ g s}^{-1} \left( \frac{\mathcal{Z}}{0.01} \right) \times \left( \frac{Q(X)}{10^{21} \text{ molecules s}^{-1}} \right) \left( \frac{m_{\text{H}_2\text{O}}}{m_X} \right). \quad (16)$$

Due to the small gas production rates required to power the accelerations of order  $10^{19}$ – $10^{21}$  molecules  $\text{s}^{-1}$ , the corresponding dust production rates are extremely small. For instance, in the case of  $\text{H}_2\text{O}$  outgassing from 1998 KY<sub>26</sub>, the dust production rate would be  $\sim 10^{-4}$  g  $\text{s}^{-1}$ . For context, (101955) Bennu exhibited  $\dot{M}_{\text{Dust}} \sim 10^{-4}$  g  $\text{s}^{-1}$ , which was only measurable in situ (Hergenrother et al. 2020). By comparison, typical observable cometary dust production

rates are  $\gtrsim 10^4$  g  $\text{s}^{-1}$  (Delsemme 1976). As a point-source analog, micron-sized dust production limits from deep stacked optical images of 11/'Oumuamua were  $\dot{M}_{\text{Dust}} \leq 0.2$ – $2$  g  $\text{s}^{-1}$  (Jewitt et al. 2017; Meech et al. 2017),  $\gtrsim 10^3 \times$  greater than these dust production rates. Therefore, in the absence of surface dust, small, rapidly rotating, and weakly outgassing bodies should not produce detectable dust activity. It is not surprising that these objects have not been identified as active asteroids (Jewitt & Hsieh 2022).

In the absence of extended tails in images, activity may be detected via drastic brightness changes in light curves. For the case of (101955) Bennu, which displayed no tail, Hergenrother et al. (2020) estimated that the dust production  $\dot{M}_{\text{Dust}} \sim 10^{-4}$  g  $\text{s}^{-1}$  would not be detectable in light curves. They estimated the detection threshold of ground-based photometric surveys as 0.1 mag, or 9.6% of its absolute magnitude. Given (101955) Bennu's average projected surface area of  $1.9 \times 10^9$  cm<sup>2</sup>, this sensitivity limit corresponds to the release of dust particles with a total area of  $1.8 \times 10^8$  cm<sup>2</sup>. The largest ejection event on January 6 produced a surface area of  $\sim 170$ – $190$  cm<sup>2</sup>. Therefore, even the largest production event recorded for (101955) Bennu would have been undetectable with ground-based observations by  $\sim 10^6$  orders of magnitude. And so, again, it is not surprising that activity has not been detected in these objects, since the implied dust production is comparable to that of (101955) Bennu. It is important to note that (101955) Bennu does not have a significant nongravitational acceleration due to particle ejection, and the activity is thought to stem from

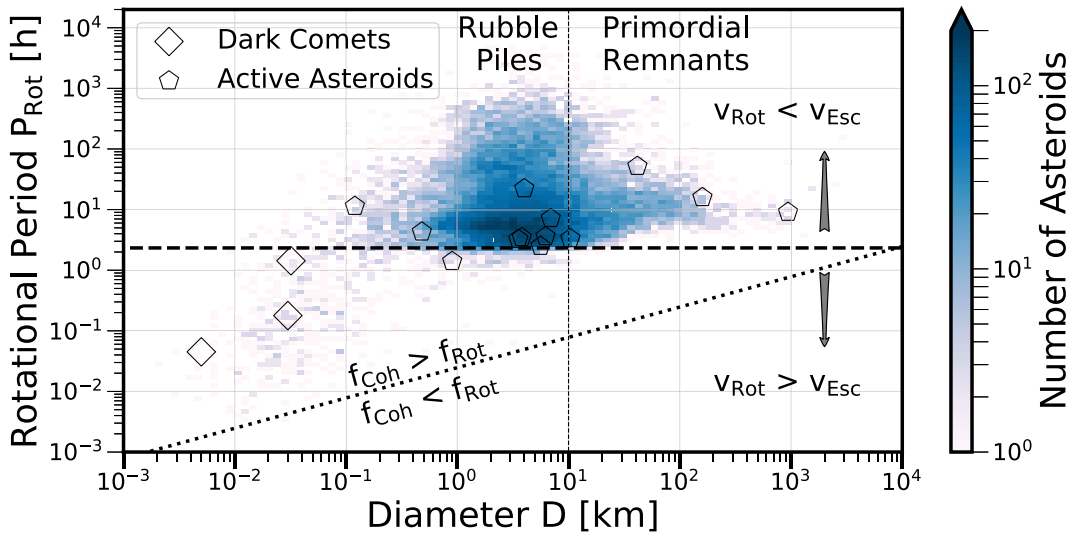


**Figure 7.** Two-dimensional histogram showing the distribution of rotational periods vs. diameters of asteroids. The critical period is shown by a dashed line, and the relationship where cohesive forces are equal to rotational forces (Equation (11) assuming  $\sigma_c = 10$  Pa,  $\rho_D = 1$  g cm $^{-3}$ , and  $R_D = 1$  mm) is indicated with a dotted line. These data are from Warner et al. (2009). Vertical dashed lines delineate the size scales of rubble piles and primordial intact remnants. Objects 1998 KY $_{26}$ , 2016 NJ $_{33}$ , and 2006 RH $_{120}$  are indicated with diamonds, while the other candidate dark comets in our sample do not have rotation periods measured. Active asteroids with sizes and rotational periods measured (Table 3) are indicated with pentagons.

other sources, such as meteoroid bombardment with a granular surface prepped by thermal fracturing (Chesley et al. 2020).

We perform an analogous calculation for 1998 KY $_{26}$ . The projected surface area of 1998 KY $_{26}$  with  $R_{\text{Nuc}} = 15$  m is  $\sim 7 \times 10^6$  cm $^2$ . We assume that the dust produced had the same properties as the particles ejected from (101955) Bennu, with a resulting projected surface area of 170–190 cm $^2$ . Because 1998 KY $_{26}$  is smaller than (101955) Bennu, the change in brightness would be  $\sim 2.5 \times 10^{-5}$ , or  $\sim 0.0025\%$  of its absolute magnitude. This is orders of magnitude below the uncertainty level (0.1 mag) of the photometric measurements obtained during the 1998 apparition (Figure 3 in Ostro et al. 1999). For the remaining objects, the extant photometric data (some of which are reported without error bars) are not sufficient to capture such brightening events (not shown). Although there has been no activity reported for any of our candidate dark comets, the dust production levels estimated here are not detectable in extant data by orders of magnitude. Moreover, even if the photometric measurements did have the absolute accuracy required to detect this level of activity, the intrinsic variation due to (i) rotation, (ii) phase variation, and (iii) changing of the geometry would mask this relatively small activity signature. To detect this level of activity photometrically, we would first require a high-precision shape model with high-fidelity information regarding the scattering properties of the surface.

### 5. Follow-up Observations

The peculiar behavior of these objects compared to known comets and asteroids makes them prime targets for follow-up observations. Given that volatile outgassing is a plausible mechanism to explain the out-of-plane nongravitational accelerations, spectroscopic observations are needed to detect or place limits on the presence of candidate volatiles (H $_2$ O, CO $_2$ , and CO) around these objects. Given the low production rates, the sensitivity of the James Webb Space Telescope (JWST) will likely be required to obtain meaningful constraints. Additionally, deep imaging is needed to improve the limits

on dust activity levels. Moreover, additional astrometric observations would help to constrain the radial acceleration  $A_1$  and may show that the nongravitational accelerations of these objects are higher than those reported in this paper.

In Figure 8, we show the solar elongation, visual magnitude, and rate of motion on the sky for 1998 KY $_{26}$ . Based on the observing constraints of JWST, 1998 KY $_{26}$  is the best candidate for observations in the near future (through 2024). Improved constraints on the nature of this object will help to resolve whether they are indeed part of a previously undescribed class of solar system bodies.

It was announced in 2020 September that Hayabusa2 will visit 1998 KY $_{26}$  after performing two swing-by maneuvers at Earth in the extended mission (Hirabayashi et al. 2021). The spacecraft is equipped (Watanabe et al. 2017) with a suite of instruments, the first being an optical navigation camera with one telescopic and two wide-angle cameras with seven filters at 0.39  $\mu\text{m}$  (*ul*-band), 0.48  $\mu\text{m}$  (*b*-band), 0.55  $\mu\text{m}$  (*v*-band), 0.59  $\mu\text{m}$  (Na), 0.70  $\mu\text{m}$  (*x*-band), 0.86  $\mu\text{m}$  (*w*-band), and 0.95  $\mu\text{m}$  (*p*-band; Kameda et al. 2015, 2017; Suzuki et al. 2018; Tatsumi et al. 2019). The thermal infrared imager is capable of measuring surface roughness and thermal emissivity and inertia via high-resolution images covering 8–12  $\mu\text{m}$  of thermal infrared emission that capture surface temperature ranges from 150 to 460 K (Arai et al. 2017; Okada et al. 2017; Takita et al. 2017). The laser altimeter (Mizuno et al. 2017; Senshu et al. 2017; Yamada et al. 2017) can detect dust grains in the vicinity of an asteroid, with a quoted sensitivity to asteroidal dust grains similar to the Hayabusa sample surrounding the target if the number density is  $>10^5$  m $^{-3}$  (Senshu et al. 2017). It is also equipped with a near-infrared spectrometer capable of obtaining spectra at near-infrared wavelengths of 1.8–3.2  $\mu\text{m}$ , designed to measure the reflectance spectra of absorption bands of hydrated and hydroxide minerals (Iwata et al. 2017). Therefore, the nature of the nongravitational acceleration of 1998 KY $_{26}$  should be definitively identified by Hayabusa2.

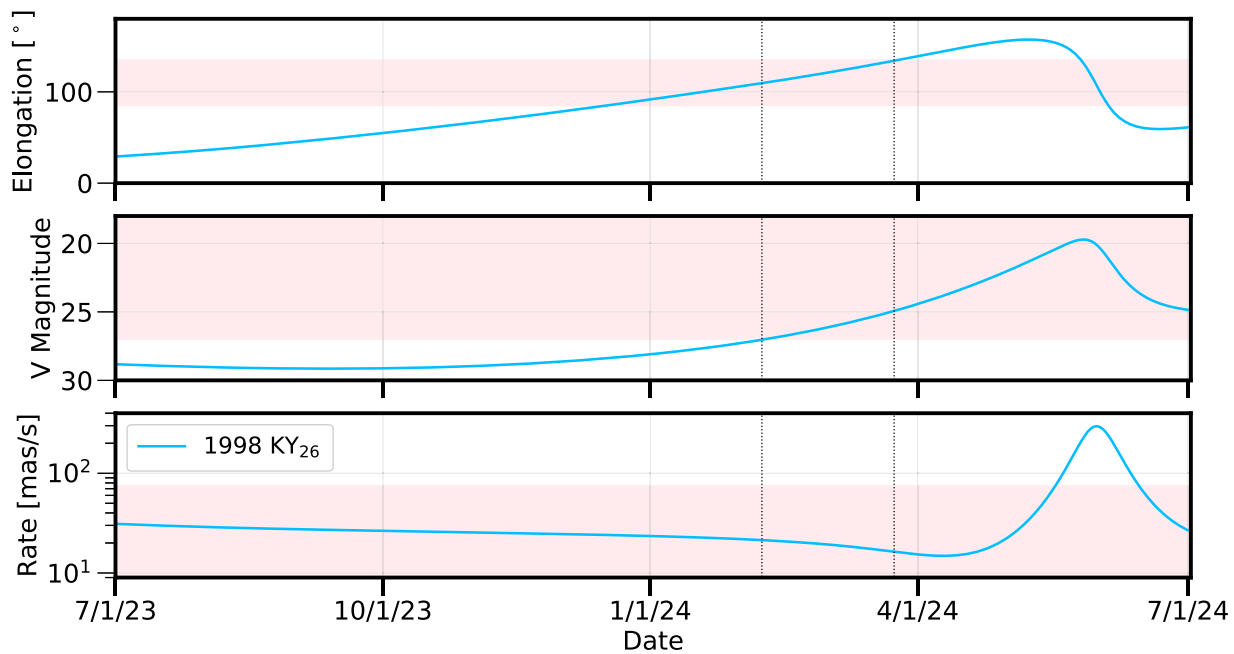


**Figure 8.** Observability of 1998 KY<sub>26</sub> with JWST from 2023 to 2024 July. We show the Sun–observer–target apparent solar elongation angle as seen from the observers’ location (top), the apparent visual magnitude (middle), and the rate of motion on the sky (bottom). The other candidate dark comets are not observable during this time period. The pink shaded region corresponds to nominal observability criteria for JWST, specifically,  $85^\circ < \text{elongation} < 135^\circ$ ,  $V \text{ mag} < 27$  mag, and rate of motion  $< 75 \text{ mas s}^{-1}$ . The vertical dotted lines indicate the time window between 2024 February and March when all three observability criteria will be satisfied.

## 6. Conclusions

In this paper, we identified five inactive objects lacking visible comae that nonetheless showed significant nongravitational acceleration in the out-of-plane direction. These objects are part of the near-Earth object population and are all characterized by nonpeculiar orbits (e.g., typical semimajor axes, eccentricity, and inclination). As a rule, these objects are small ( $R_{\text{Nuc}} \sim 3\text{--}16 \text{ m}$ ) and have rapid rotation periods (when measured).

While the nature of these objects remains uncertain, we showed that an outgassing mechanism can plausibly explain the out-of-plane nongravitational acceleration without producing a visible dust coma. This is largely due to the small size of the bodies, which means that (i) relatively low gas production rates are needed to explain the accelerations, and (ii) the nuclei may not have surface dust, possibly due to continual cleansing from outgassing. For objects that have lost their surface dust, the only contribution to dust activity is the entrainment of dust from the subsurface during ice sublimation. Based on the gas production rates inferred for the bodies, we show that the production of dust via entrainment is extremely small and well within the observational limits. It is possible that these objects are solar system analogs to II/‘Oumuamua, which also exhibited a nongravitational acceleration and lack of cometary activity.

Follow-up observations are critical to understanding the nature of these unusual objects, potentially members of a new class of “dark comets” in the solar system. In particular, observations with JWST would reveal whether their nongravitational accelerations are in fact due to volatile outgassing (e.g.,  $\text{H}_2\text{O}$ ,  $\text{CO}_2$ , or  $\text{CO}$ ) or whether a new mechanism is needed to explain their peculiar properties.

We thank Dave Jewitt, John Noonan, Masatoshi Hirabayashi, Dong Lai, Fred Adams, Nikole Lewis, Konstantin Batygin,

Samantha Trumbo, Gregory Laughlin, Juliette Becker, Mike Brown, Ngoc Truong, J. T. Laune, and Jonathan Lunine for useful conversations and suggestions. We thank Dave Jewitt and Henry Hsieh for compiling the data in Table 3 and granting permission to reproduce it. We thank the scientific editor Faith Vilas for securing constructive and rapid referee reports. We thank the two anonymous reviewers for insightful comments and constructive suggestions that strengthened the scientific content of this manuscript.

D.Z.S. acknowledges financial support from National Science Foundation grant No. AST-17152, NASA grant No. 80NSSC19K0444, and NASA contract NNX17AL71A from the NASA Goddard Space Flight Center. Part of this research was carried out at the Jet Propulsion Laboratory, California Institute of Technology, under a contract with the National Aeronautics and Space Administration (80NM0018D0004). D. V. was supported by the Czech Science Foundation, grant GA21-11058S. This work was partially supported by NASA grant No. NNX17AH06G (PI: N. Moskovitz) issued through the Near-Earth Object Observations program to the Mission Accessible Near-Earth Object Survey (MANOS). D.J.T. acknowledges support from NASA grant 80NSSC21K0807. The Arecibo planetary radar observation presented in this work was supported by the National Aeronautics and Space Administration’s (NASA) Near-Earth Object Observations program through grant No. NNX13AQ46G awarded to the Universities Space Research Association (USRA). Reduction of the data was performed under grant No. 80NSSC18K1098 awarded to the University of Central Florida (UCF). The Arecibo Observatory is a facility of the National Science Foundation (NSF) operated under cooperative agreement by UCF, Yang Enterprises, Inc., and Universidad Ana G. Méndez. This paper is partially based on observations collected at the European Southern Observatory under ESO program 105.202E.002.

### Appendix A

#### Rotation Period of 2016 NJ<sub>33</sub>

For 2016 NJ<sub>33</sub>, we estimate the rotational period using one continuous-wave (CW) observation obtained with the Arecibo Observatory planetary radar system, shown in Figure 9. The CW spectrum shows a bandwidth of  $0.50 \pm 0.02$  Hz. Using the relation linking the bandwidth of a CW spectrum and the rotation period (see Virkki et al. 2022 for more information on CW radar observations and their analysis), we estimate that the rotation period of 2016 NJ<sub>33</sub> is between 0.41 and 1.99 hr with a mean of 1.43 hr with  $3\sigma$  confidence. We obtained this result by simulating random pole orientations and a normal distribution of the bandwidth ( $0.50 \pm 0.02$  Hz) and diameter ( $32 \pm 3$  m). This estimation of the rotational period should be treated with caution because (i) we only have one observation of the object, (ii) an observation very close to pole-on geometry would result in a very fast rotation period, and (iii) we assume a spherical nucleus, and if the object is highly elongated, a very different cross section would be allowable. However, there is a low probability of randomly observing the object pole-on.

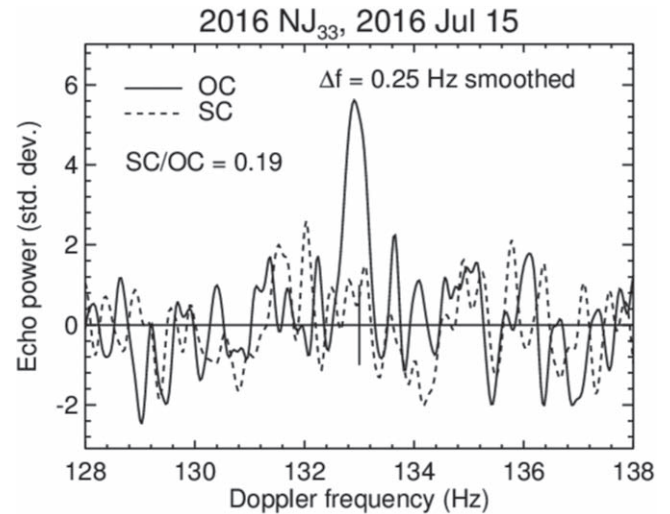


**Figure 9.** Radar CW spectrum of 2016 NJ<sub>33</sub> taken with the Arecibo Observatory. The CW spectrum shows that the minimum rotation period should be between 0.41 and 1.99 hr. Because we have no information regarding the pole orientation of the object, it is possible that the rotational period is much more rapid. The low SC/OC ratio excludes an E-type classification (Benner et al. 2008). Reproduced from <https://www.naic.edu/~pradar/asteroids/2016NJ33/2016NJ33.2016Jul15.s0p25Hz.cw.gif>.

## Appendix B

### Data for Active Asteroids and Cometary Nuclei

Table 1 lists relevant properties of the dark comet candidates. In Table 2, we show the relevant data and references for comets

with measured nucleus rotation rates and sizes. Table 3 is reproduced from Jewitt & Hsieh (2022) and lists active asteroid properties.

**Table 3**  
Properties of the Currently Known Active Asteroids

Object Name	$a$ (au)	$e$	$i$ (deg)	$H$ (mag)	$R_{\text{Nuc}}$ (m)	$P_{\text{Rot}}$ (hr)	Reference
(1) Ceres	2.766	0.078	10.588	3.53	469.7	9.07	Küppers et al. (2014) Park et al. (2016)
(493) Griseldis	3.116	0.176	15.179	10.97	20.78	51.94	Tholen et al. (2015)
(596) Scheila	2.929	0.163	14.657	8.93	79.86	15.85	Ishiguro et al. (2011)
(2201) Oljato	2.174	0.713	2.522	15.25	0.90	>26.	Russell et al. (1984) Tedesco et al. (2004)
(3200) Phaethon	1.271	0.890	22.257	14.32	3.13	3.60	Jewitt & Li (2010) Ansdell et al. (2014)
(6478) Gault	2.305	0.193	22.812	14.81	2.8	2.49	Devogèle et al. (2021)
(62412) 2000 SY <sub>178</sub>	3.159	0.079	4.738	13.74	5.19	3.33	Sheppard & Trujillo (2015)
(101955) Bennu	1.126	0.204	6.035	20.21	0.24	4.29	Lauretta et al. (2019)
107P/(4015) Wilson–Harrington	2.625	0.632	2.799	16.02	3.46	7.15	Fernández et al. (1997) Licandro et al. (2009) Urakawa et al. (2011)
133P/(7968) Elst–Pizarro	3.165	0.157	1.389	15.49	1.9	3.47	Hsieh et al. (2009)
176P/(118401) LINEAR	3.194	0.193	0.235	15.10	2.0	22.23	Hsieh et al. (2009)
233P/La Sagra (P/2005 JR <sub>71</sub> )	3.033	0.411	11.279	16.6	1.5	...	Mainzer et al. (2010)
238P/Read (P/2005 U1)	3.162	0.253	1.266	19.05	0.4	...	Hsieh et al. (2011)
259P/Garradd (P/2008 R1)	2.727	0.342	15.899	19.71	0.30	...	MacLennan & Hsieh (2012)
288P/(300163) 2006 VW <sub>139</sub>	3.051	0.201	3.239	17.8, 18.2	0.9, 0.6	...	Agarwal et al. (2020)
311P/PANSTARRS (P/2013 P5)	2.189	0.116	4.968	19.14	0.2	>5.4	Jewitt et al. (2018)
313P/Gibbs (P/2014 S4)	3.154	0.242	10.967	17.1	1.0	...	Hsieh et al. (2015)
324P/La Sagra (P/2010 R2)	3.098	0.154	21.400	18.4	0.55	...	Hsieh & Sheppard (2015)
331P/Gibbs (P/2012 F5)	3.005	0.042	9.739	17.33	1.77	3.24	Drahus et al. (2015)
354P/LINEAR (P/2010 A2)	2.290	0.125	5.256	...	0.06	11.36	Snodgrass et al. (2010)
358P/PANSTARRS (P/2012 T1)	3.155	0.236	11.058	19.5	0.32	...	Hsieh et al. (2018)
426P/PANSTARRS (P/2019 A7)	3.188	0.161	17.773	17.1	1.2	...	...
427P/ATLAS (P/2017 S5)	3.171	0.313	11.849	18.91	0.45	1.4	Jewitt et al. (2019)
432P/PANSTARRS (P/2021 N4)	3.045	0.244	10.067	>18.2	<0.7	...	...
433P/(248370) 2005 QN <sub>173</sub>	3.067	0.226	0.067	16.32	1.6	...	Hsieh et al. (2021b) Novaković et al. (2022)
P/2013 R3 (Catalina-PANSTARRS)	3.033	0.273	0.899	...	~0.2	...	Jewitt et al. (2014)
P/2015 X6 (PANSTARRS)	2.755	0.170	4.558	>18.2	<0.7	...	Moreno et al. (2016a)
P/2016 G1 (PANSTARRS)	2.583	0.210	10.968	...	<0.4	...	Moreno et al. (2016b) Hainaut et al. (2019)
P/2016 J1-A/B (PANSTARRS)	3.172	0.228	14.330	...	<0.4, <0.9	...	Moreno et al. (2017)
P/2017 S9 (PANSTARRS)	3.156	0.305	14.138	>17.8	<0.8	...	Weryk et al. (2017)
P/2018 P3 (PANSTARRS)	3.007	0.416	8.909	>18.6	<0.6	...	Weryk et al. (2018)
P/2019 A3 (PANSTARRS)	3.147	0.265	15.367	>19.3	<0.4	...	Weryk et al. (2019)
P/2019 A4 (PANSTARRS)	2.614	0.090	13.319	...	0.17	...	Moreno et al. (2021)
P/2020 O1 (Lemmon-PANSTARRS)	2.647	0.120	5.223	>17.7	<0.9	...	...
P/2021 A5 (PANSTARRS)	3.047	0.140	18.188	...	0.15	...	Moreno et al. (2021)
P/2021 L4 (PANSTARRS)	3.165	0.119	16.963	>15.8	<2.2	...	...
P/2021 R8 (Sheppard)	3.019	0.294	2.203	...	...	...	...

**Note.** This table is reproduced from Jewitt & Hsieh (2022) with permission from the authors.

## ORCID iDs

Darryl Z. Seligman  <https://orcid.org/0000-0002-0726-6480>  
 Davide Farnocchia  <https://orcid.org/0000-0003-0774-884X>  
 Marco Micheli  <https://orcid.org/0000-0001-7895-8209>  
 David Vokrouhlický  <https://orcid.org/0000-0002-6034-5452>  
 Aster G. Taylor  <https://orcid.org/0000-0002-0140-4475>  
 Steven R. Chesley  <https://orcid.org/0000-0003-3240-6497>  
 Jennifer B. Bergner  <https://orcid.org/0000-0002-8716-0482>  
 Peter Vereš  <https://orcid.org/0000-0002-5396-946X>  
 Olivier R. Hainaut  <https://orcid.org/0000-0001-6952-9349>  
 Karen J. Meech  <https://orcid.org/0000-0002-2058-5670>  
 Maxime Devogele  <https://orcid.org/0000-0002-6509-6360>  
 Petr Pravec  <https://orcid.org/0000-0001-8434-9776>  
 David J. Tholen  <https://orcid.org/0000-0003-0773-1888>  
 Robert Weryk  <https://orcid.org/0000-0002-0439-9341>  
 Edgard G. Rivera-Valentín  <https://orcid.org/0000-0002-4042-003X>  
 Benjamin N. L. Sharkey  <https://orcid.org/0000-0003-1383-1578>

## References

- Abell, P. A., Fernández, Y. R., Pravec, P., et al. 2005, *Icar*, **179**, 174  
 Agarwal, J., Kim, Y., Jewitt, D., et al. 2020, *A&A*, **643**, A152  
 A'Hearn, M. F., Campins, H., Schleicher, D. G., & Millis, R. L. 1989, *ApJ*, **347**, 1155  
 A'Hearn, M. F., Belton, M. J. S., Delamere, W. A., et al. 2005, *Sci*, **310**, 258  
 Albarède, F. 2009, *Natur*, **461**, 1227  
 Almeida-Fernandes, F., & Rocha-Pinto, H. J. 2018, *MNRAS*, **480**, 4903  
 Ansdell, M., Meech, K. J., Hainaut, O., et al. 2014, *ApJ*, **793**, 50  
 Appenzeller, I., Fricke, K., Fürtig, W., et al. 1998, *Msngr*, **94**, 1  
 Arai, T., Nakamura, T., Tanaka, S., et al. 2017, *SSRv*, **208**, 239  
 Arai, T., Yoshida, F., Kobayashi, M., et al. 2021, *LPSC*, **52**, 1896  
 Asher, D. J., Bailey, M. E., Hahn, G., & Steel, D. I. 1994, *MNRAS*, **267**, 26  
 Bannister, M. T., Schwamb, M. E., Fraser, W. C., et al. 2017, *ApJL*, **851**, L38  
 Barnouin, O. S., Daly, M. G., Palmer, E. E., et al. 2019, *NatGe*, **12**, 247  
 Belton, M. J. S., Thomas, P., Li, J.-Y., et al. 2013, *Icar*, **222**, 595  
 Belton, M. J. S., Hainaut, O. R., Meech, K. J., et al. 2018, *ApJL*, **856**, L21  
 Benner, L. A., Ostro, S. J., Magri, C., et al. 2008, *Icar*, **198**, 294  
 Bertini, I. 2011, *P&SS*, **59**, 365  
 Binzel, R. P., Xu, S., Bus, S. J., & Bowell, E. 1992, *Sci*, **257**, 779  
 Birnstiel, T., Dullemond, C. P., & Brauer, F. 2010, *A&A*, **513**, A79  
 Bodewits, D., Noonan, J. W., Feldman, P. D., et al. 2020, *NatAs*, **4**, 867  
 Boehnhardt, H., Schulz, R., Tozzi, G. P., Rauer, H., & Sekanina, Z. 1996, *IAUC*, **6495**, 2  
 Bolin, B. T., Weaver, H. A., Fernandez, Y. R., et al. 2018, *ApJL*, **852**, L2  
 Bottke, W. F., Brož, M., O'Brien, D. P., et al. 2015, in *Asteroids IV*, ed. P. Michel, F. E. DeMeo, & W. F. Bottke (Tucson, AZ: Univ. Arizona Press), **701**  
 Bottke, W. F., Durda, D. D., Nesvorný, D., et al. 2005, *Icar*, **175**, 111  
 Bottke, W. F., Moorhead, A. V., Connolly, H. C., et al. 2020, *JGRE*, **125**, e06282  
 Brasser, R., & Wang, J. H. 2015, *A&A*, **573**, A102  
 Cheng, A. F., Izenberg, N., Chapman, C. R., & Zuber, M. T. 2002, *M&PS*, **37**, 1095  
 Chesley, S. R., Farnocchia, D., Pravec, P., & Vokrouhlický, D. 2016, in *IAU Symp. Asteroids: New Observations, New Models*, ed. S. R. Chesley et al. (Cambridge: Cambridge Univ. Press), **250**  
 Chesley, S. R., French, A. S., Davis, A. B., et al. 2020, *JGRE*, **125**, e06363  
 Chyba, C. F. 1990, *Natur*, **343**, 129  
 Cremonese, G., Fulle, M., Cambianica, P., et al. 2020, *ApJL*, **893**, L12  
 Delsemme, A. H. 1976, in *Interplanetary Dust and Zodiacal Light, Lecture Notes in Physics*, Vol. 48, ed. H. Elsaesser & H. Fechtig (Berlin: Springer), **314**  
 Dermawan, B., Nakamura, T., & Yoshida, F. 2011, *PASJ*, **63**, 555  
 Devogèle, M., Ferrais, M., Jehin, E., et al. 2021, *MNRAS*, **505**, 245  
 Drahus, M., Guzik, P., Waniak, W., et al. 2018, *NatAs*, **2**, 407  
 Drahus, M., Waniak, W., Tendulkar, S., et al. 2015, *ApJL*, **802**, L8  
 Eisner, N., Knight, M. M., & Schleicher, D. G. 2017, *AJ*, **154**, 196  
 Elst, E. W., Pizarro, O., Pollas, C., et al. 1996, *IAUC*, **6456**, 1  
 Farnocchia, D., Chesley, S. R., Milani, A., Gronchi, G. F., & Chodas, P. W. 2015, in *Asteroids IV*, ed. P. Michel, F. E. DeMeo, & W. F. Bottke (Tucson, AZ: Univ. Arizona Press), **815**  
 Farnocchia, D., Tholen, D. J., Micheli, M., et al. 2017, *AAS/DPS Meeting*, **49**, 100.09  
 Fedorets, G., Micheli, M., Jedicke, R., et al. 2020, *AJ*, **160**, 277  
 Farnocchia, D., Chesley, S. R., Takahashi, Y., et al. 2021, *Icar*, **369**, 114594  
 Farnocchia, D., Seligman, D. Z., Granvik, M., et al. 2023, *PSJ*, **4**, 29  
 Feng, F., & Jones, H. R. A. 2018, *ApJL*, **852**, L27  
 Ferellec, L., Snodgrass, C., Fitzsimmons, A., et al. 2022, *MNRAS*, **518**, 2373  
 Fernández, Y. R., Jewitt, D. C., & Sheppard, S. S. 2005a, *AJ*, **130**, 308  
 Fernández, Y. R., Lowry, S. C., Weissman, P. R., et al. 2005b, *Icar*, **175**, 194  
 Fernández, Y. R., McFadden, L. A., Lisse, C. M., Helin, E. F., & Chamberlin, A. B. 1997, *Icar*, **128**, 114  
 Fitzsimmons, A., Snodgrass, C., Rozitis, B., et al. 2018, *NatAs*, **2**, 133  
 Fraser, W. C., Pravec, P., Fitzsimmons, A., et al. 2018, *NatAs*, **2**, 383  
 Fujiwara, A., Kawaguchi, J., Yeomans, D. K., et al. 2006, *Sci*, **312**, 1330  
 Gaidos, E., Williams, J., & Kraus, A. 2017, *RNAAS*, **1**, 13  
 Granvik, M., Vaubaillon, J., & Jedicke, R. 2012, *Icar*, **218**, 262  
 Granvik, M., Morbidelli, A., Jedicke, R., et al. 2018, *Icar*, **312**, 181  
 Greenberg, A. H., Margot, J.-L., Verma, A. K., Taylor, P. A., & Hodge, S. E. 2020, *AJ*, **159**, 92  
 Gustafson, B. A. S. 1989, *A&A*, **225**, 533  
 Guzik, P., Drahus, M., Rusek, K., et al. 2020, *NatAs*, **4**, 53  
 Hahn, J. M., & Malhotra, R. 1999, *AJ*, **117**, 3041  
 Hainaut, O. R., Micheli, M., Cano, J. L., et al. 2021, *A&A*, **653**, A124  
 Hainaut, O. R., Kleyna, J. T., Meech, K. J., et al. 2019, *A&A*, **628**, A48  
 Hallatt, T., & Wiegert, P. 2020, *AJ*, **159**, 147  
 Hanuš, J., Delbo, M., Vokrouhlický, D., et al. 2016, *A&A*, **592**, A34  
 Harmon, J. K., Nolan, M. C., Howell, E. S., Giorgini, J. D., & Taylor, P. A. 2011, *ApJL*, **734**, L2  
 Harrington-Pinto, O., Womack, M., Fernandez, Y., & Bauer, J. 2022, *PSJ*, **3**, 247  
 Harris, A. W. 1979, *Icar*, **40**, 145  
 Harris, A. W. 1996, *LPSC*, **27**, 493  
 Harris, A. W., & Burns, J. A. 1979, *Icar*, **40**, 115  
 Hergenrother, C. W., Maleszewski, C. K., Nolan, M. C., et al. 2019, *NatCo*, **10**, 1291  
 Hergenrother, C. W., Maleszewski, C., Li, J. Y., et al. 2020, *JGRE*, **125**, e06381  
 Hicks, M., & Thackeray, B. 2016, *ATel*, **8905**, 1  
 Hirabayashi, M., Scheeres, D. J., Sánchez, D. P., & Gabriel, T. 2014, *ApJL*, **789**, L12  
 Hirabayashi, M., Mimasu, Y., Sakatani, N., et al. 2021, *AdSpR*, **68**, 1533  
 Hsieh, C.-H., Laughlin, G., & Arce, H. G. 2021a, *ApJ*, **917**, 20  
 Hsieh, H. H., Chandler, C. O., Denneau, L., et al. 2021b, *ApJL*, **922**, L9  
 Hsieh, H. H. 2017, *RSPTA*, **375**, 20160259  
 Hsieh, H. H., Ishiguro, M., Knight, M. M., et al. 2018, *AJ*, **156**, 39  
 Hsieh, H. H., & Jewitt, D. 2006, *Sci*, **312**, 561  
 Hsieh, H. H., Jewitt, D., & Fernández, Y. R. 2009, *ApJL*, **694**, L111  
 Hsieh, H. H., Jewitt, D. C., & Fernández, Y. R. 2004, *AJ*, **127**, 2997  
 Hsieh, H. H., Meech, K. J., & Pittichová, J. 2011, *ApJL*, **736**, L18  
 Hsieh, H. H., & Sheppard, S. S. 2015, *MNRAS*, **454**, L81  
 Hsieh, H. H., Hainaut, O., Novaković, B., et al. 2015, *ApJL*, **800**, L16  
 Hui, M.-T., & Jewitt, D. 2017, *AJ*, **153**, 80  
 Hui, M.-T., & Li, J. 2017, *AJ*, **153**, 23  
 Hui, M.-T., Ye, Q.-Z., Föhring, D., Hung, D., & Tholen, D. J. 2020, *AJ*, **160**, 92  
 Ishiguro, M., Hanayama, H., Hasegawa, S., et al. 2011, *ApJL*, **740**, L11  
 Iwata, T., Kitazato, K., Abe, M., et al. 2017, *SSRv*, **208**, 317  
 Jewitt, D. 2005, *AJ*, **129**, 530  
 Jewitt, D. 2012, *AJ*, **143**, 66  
 Jewitt, D. 2021, *AJ*, **161**, 261  
 Jewitt, D., Agarwal, J., Li, J., et al. 2014, *ApJL*, **784**, L8  
 Jewitt, D., & Hsieh, H. H. 2022, arXiv:2203.01397  
 Jewitt, D., Hui, M.-T., Kim, Y., et al. 2020, *ApJL*, **888**, L23  
 Jewitt, D., & Li, J. 2010, *AJ*, **140**, 1519  
 Jewitt, D., Li, J., & Agarwal, J. 2013, *ApJL*, **771**, L36  
 Jewitt, D., & Luu, J. 1989, *AJ*, **97**, 1766  
 Jewitt, D., & Luu, J. 2019, *ApJL*, **886**, L29  
 Jewitt, D., Luu, J., Rajagopal, J., et al. 2017, *ApJL*, **850**, L36  
 Jewitt, D., & Seligman, D. Z. 2022, *ARA&A*, arXiv:2209.08182, in press  
 Jewitt, D., Weaver, H., Mutchler, M., et al. 2018, *AJ*, **155**, 231  
 Jewitt, D., Kim, Y., Rajagopal, J., et al. 2019, *AJ*, **157**, 54  
 Kameda, S., Suzuki, H., Cho, Y., et al. 2015, *AdSpR*, **56**, 1519  
 Kameda, S., Suzuki, H., Takamatsu, T., et al. 2017, *SSRv*, **208**, 17

- Kim, Y., Jewitt, D., Mutchler, M., et al. 2020, *ApJL*, **895**, L34
- Knight, M. M., Protopapa, S., Kelley, M. S. P., et al. 2017, *ApJL*, **851**, L31
- Knight, M. M., Schleicher, D. G., Farnham, T. L., Schwietzman, E. W., & Christensen, S. R. 2012, *AJ*, **144**, 153
- Kokotanekova, R., Snodgrass, C., Lacerda, P., et al. 2017, *MNRAS*, **471**, 2974
- Krüger, H., Strub, P., Srama, R., et al. 2019, *P&SS*, **172**, 22
- Küppers, M., O'Rourke, L., Bockelée-Morvan, D., et al. 2014, *Natur*, **505**, 525
- Kwiatkowski, T., Kryszyńska, A., Polińska, M., et al. 2009, *A&A*, **495**, 967
- Lauretta, D. S., Hergenrother, C. W., Chesley, S. R., et al. 2019, *Sci*, **366**, eaay3544
- Li, J., & Jewitt, D. 2013, *AJ*, **145**, 154
- Licandro, J., Popescu, M., de León, J., et al. 2018, *A&A*, **618**, A170
- Licandro, J., Campins, H., Kelley, M., et al. 2009, *A&A*, **507**, 1667
- Lowry, S. C., & Weissman, P. R. 2007, *Icar*, **188**, 212
- MacLennan, E. M., & Hsieh, H. H. 2012, *ApJL*, **758**, L3
- Mainzer, A., Read, M. T., Scottii, J. V., Ryan, W. H., & Ryan, E. V. 2010, *IAUC*, **9117**, 1
- Mamajek, E. 2017, *RNAAS*, **1**, 21
- Marsden, B. G., Sekanina, Z., & Yeomans, D. K. 1973, *AJ*, **78**, 211
- Mashchenko, S. 2019, *MNRAS*, **489**, 3003
- Masiero, J. 2017, arXiv:1710.09977
- Masiero, J. R., Davidsson, B. J. R., Liu, Y., Moore, K., & Tuite, M. 2021, *PSJ*, **2**, 165
- McNeill, A., Trilling, D. E., & Mommert, M. 2018, *ApJL*, **857**, L1
- Meech, K. J., Yang, B., Kleyana, J., et al. 2016, *SciA*, **2**, e1600038
- Meech, K. J., Weryk, R., Micheli, M., et al. 2017, *Natur*, **552**, 378
- Micheli, M., Tholen, D. J., & Elliott, G. T. 2012, *NewA*, **17**, 446
- Micheli, M., Tholen, D. J., & Elliott, G. T. 2013, *Icar*, **226**, 251
- Micheli, M., Tholen, D. J., & Elliott, G. T. 2014, *ApJL*, **788**, L1
- Micheli, M., Farnocchia, D., Meech, K. J., et al. 2018, *Natur*, **559**, 223
- Mizuno, T., Kase, T., Shiina, T., et al. 2017, *SSRv*, **208**, 33
- Molaro, J. L., Hergenrother, C. W., Chesley, S. R., et al. 2020, *JGRE*, **125**, e06325
- Mommert, M., Hora, J. L., Farnocchia, D., et al. 2014a, *ApJ*, **786**, 148
- Mommert, M., Farnocchia, D., Hora, J. L., et al. 2014b, *ApJL*, **789**, L22
- Moreno, F., Licandro, J., Cabrera-Lavers, A., Morate, D., & Guirado, D. 2021, *MNRAS*, **506**, 1733
- Moreno, F., Licandro, J., Cabrera-Lavers, A., & Pozuelos, F. J. 2016a, *ApJ*, **826**, 137
- Moreno, F., Licandro, J., Cabrera-Lavers, A., & Pozuelos, F. J. 2016b, *ApJL*, **826**, L22
- Moreno, F., Pozuelos, F. J., Novaković, B., et al. 2017, *ApJL*, **837**, L3
- Moro-Martín, A. 2022, arXiv:2205.04277
- Mottola, S., Lowry, S., Snodgrass, C., et al. 2014, *A&A*, **569**, L2
- Nakano, R., & Hirabayashi, M. 2020, *ApJL*, **892**, L22
- Novaković, B., Pavela, D., Hsieh, H. H., & Marčeta, D. 2022, *MNRAS*, **516**, 757
- Okada, T., Fukuhara, T., Tanaka, S., et al. 2017, *SSRv*, **208**, 255
- Ostro, S. J., Pravec, P., Benner, L. A. M., et al. 1999, *Sci*, **285**, 557
- Owen, T., & Bar-Nun, A. 1995, *Icar*, **116**, 215
- Park, R. S., Konopliv, A. S., Bills, B. G., et al. 2016, *Natur*, **537**, 515
- Podolak, M., & Herman, G. 1985, *Icar*, **61**, 267
- Pravec, P., & Harris, A. W. 2007, *Icar*, **190**, 250
- Prialnik, D., & Bar-Nun, A. 1988, *Icar*, **74**, 272
- Rozitis, B., MacLennan, E., & Emery, J. P. 2014, *Natur*, **512**, 174
- Russell, C. T., Aroian, R., Arghavani, M., & Nock, K. 1984, *Sci*, **226**, 43
- Sánchez, P., & Scheeres, D. J. 2020, *Icar*, **338**, 113443
- Scheeres, D. J., Hartzell, C. M., Sánchez, P., & Swift, M. 2010, *Icar*, **210**, 968
- Senshu, H., Oshigami, S., Kobayashi, M., et al. 2017, *SSRv*, **208**, 65
- Shannon, A., Jackson, A. P., Veras, D., & Wyatt, M. 2015, *MNRAS*, **446**, 2059
- Sheppard, S. S., & Trujillo, C. 2015, *AJ*, **149**, 44
- Sierks, H., Barbieri, C., Lamy, P. L., et al. 2015, *Sci*, **347**, aaa1044
- Snodgrass, C., Tubiana, C., Vincent, J.-B., et al. 2010, *Natur*, **467**, 814
- Snodgrass, C., Agarwal, J., Combi, M., et al. 2017, *A&ARv*, **25**, 5
- Sonnett, S., Kleyana, J., Jedicke, R., & Masiero, J. 2011, *Icar*, **215**, 534
- Suzuki, H., Yamada, M., Kouyama, T., et al. 2018, *Icar*, **300**, 341
- Takita, J., Senshu, H., & Tanaka, S. 2017, *SSRv*, **208**, 287
- Tatsumi, E., Kouyama, T., Suzuki, H., et al. 2019, *Icar*, **325**, 153
- Taylor, P. A., Rivera-Valentín, E. G., Benner, L. A. M., et al. 2019, *P&SS*, **167**, 1
- Tedesco, E. F., Noah, P. V., Noah, M., & Price, S. D. 2004, NASA Planetary Data System, IRAS Minor Planet Survey V6.0
- Tholen, D. J., Sheppard, S. S., & Trujillo, C. A. 2015, AAS/DPS Meeting, **47**, 414.03
- Toth, I. 2000, *A&A*, **360**, 375
- Trilling, D. E., Mommert, M., Hora, J. L., et al. 2018, *AJ*, **156**, 261
- Urakawa, S., Okumura, S.-i., Nishiyama, K., et al. 2011, *Icar*, **215**, 17
- Virkki, A. K., Marshall, S. E., Venditti, F. C. F., et al. 2022, *PSJ*, **3**, 222
- Vokrouhlický, D., Bottke, W. F., Chesley, S. R., Scheeres, D. J., & Statler, T. S. 2015, in Asteroids IV, ed. P. Michel, F. E. DeMeo, & W. F. Bottke (Tucson, AZ: Univ. Arizona Press), 509
- Vokrouhlický, D., & Milani, A. 2000, *A&A*, **362**, 746
- Vokrouhlický, D., Milani, A., & Chesley, S. R. 2000, *Icar*, **148**, 118
- Walsh, K. J. 2018, *ARA&A*, **56**, 593
- Wang, J. H., & Brasser, R. 2014, *A&A*, **563**, A122
- Warner, B. D. 2016, *MPBu*, **43**, 240
- Warner, B. D., Harris, A. W., & Pravec, P. 2009, *Icar*, **202**, 134
- Watanabe, S., Hirabayashi, M., Hirata, N., et al. 2019, *Sci*, **364**, 268
- Watanabe, S.-i., Tsuda, Y., Yoshikawa, M., et al. 2017, *SSRv*, **208**, 3
- Weryk, R., Wainscoat, R., Ramanjooloo, Y., Woodworth, D., & Micheli, M. 2018, *CBET*, **4548**, 1
- Weryk, R., Wainscoat, R., Woodworth, D., & Prunet, S. 2019, *CBET*, **4598**, 1
- Weryk, R., Wainscoat, R. J., Wipper, C., & Micheli, M. 2017, *CBET*, **4448**, 1
- Whipple, F. L. 1950, *ApJ*, **111**, 375
- Whipple, F. L. 1951, *ApJ*, **113**, 464
- Williams, G. V., Sato, H., Sarneczky, K., et al. 2017, *CBET*, **4450**, 1
- Williams, I. P., & Wu, Z. 1993, *MNRAS*, **262**, 231
- Wisniewski, W. Z. 1990, *Icar*, **86**, 52
- Yamada, R., Senshu, H., Namiki, N., et al. 2017, *SSRv*, **208**, 49
- Yang, B., Li, A., Cordiner, M. A., et al. 2021, *NatAs*, **5**, 586
- Ye, Q.-Z., Zhang, Q., Kelley, M. S. P., & Brown, P. G. 2017, *ApJL*, **851**, L5